BRNO UNIVERSITY OF TECHNOLOGY
VYSOKÉ UČENÍ TECHNICKÉ V BRNĚ

CENTRAL EUROPEAN INSTITUTE OF TECHNOLOGY
STŘEDOEVROPSKÝ TECHNOLOGICKÝ INSTITUT

# 2D MOLECULAR SYSTEMS AT SURFACES

2D MOLEKULÁRNÍ SYSTÉMI NA POVRŠÍCH

TEZE DIZERTAČNÍ PRÁCE
SHORT VERSION OF DOCTORAL THESIS

AUTHOR
AUTOR PRÁCE
Ing. LUKÁŠ KORMOŠ

SUPERVISOR
VEDOUCÍ PRÁCE
doc. Ing. JAN ČECHAL, Ph.D.

BRNO 2020

**Abstrakt**
Molekulárne systémy predstavujú jeden zo smerov súčasného výskumu nových nanoelektronických zariadení. Organické molekuly nachádzajú uplatnenie v rôznych aplikáciách, ako sú napríklad solárne články, displeje alebo kvantové počítače. Rast vysokokvalitných molekulárnych vrstiev s požadovanými vlastnosťami často vyžaduje využitie samousporiadavaných štruktúr, hlboké pochopenie rozhrania kovu a organických molekúl a tiež dynamiky rastu molekulárnych vrstiev. Predkladaná práca sa zaoberá predovšetkým samousporadanými štruktúrami bifenyl-dikarboxylovej kyseliny (BDA) na Cu (1 0 0) a Ag (1 0 0), ktoré boli skúmané v UHV s využitím STM, XPS a LEEM. V prípade BDA-Ag je podrobne opísaných niekoľko chemicky a štrukturálne odlišných molekulárnych fáz. Ďalej boli BDA a TCNQ molekuly skúmané na grafene pripravenom na Ir (1 1 1). Okrem toho sa organo-kovové systémy syntetizovali depozíciou atómov Ni a Fe s molekulami TCNQ a BDA. Originálna práca naviac zahurnuje povrchovú syntézu grafénových nanoribonov (7-AGNR) na špecificky štrukturovanom substráte Au (16 14 15) z prekurzorových molekúl DBBA. Rekonštrukcia povrchu po raste bola analyzovaná pomocou STM a elektronické vlastnosti 7-AGNRs pomocou ARPES.

**Summary**
Molecular systems represent one direction of the current research in novel nano-electronic devices. Organic molecules are considered in various applications such as solar cells, displays or quantum computing. Growth of high-quality molecular layers with desired properties often employs self-assembled structures and requires a deep understanding of metal-organic interface and dynamics of the molecular layer growth. Work presented in the thesis is in the beginning focused on self-assembly of biphenyl-dicarboxylic acid (BDA) on Cu (1 0 0) and Ag (1 0 0) studied in UHV utilising STM, XPS and LEEM. In the case of BDA/Ag, multiple chemically and structurally distinct molecular phases are described in detail. Next, the BDA and TCNQ self-assembly is studied on graphene grown on Ir (1 1 1). In addition, metal-organic systems were synthesised by deposition of additional Ni and Fe atoms with TCNQ and BDA molecules on graphene. Original work also includes on-surface synthesis of graphene nanoribbons (7-AGNR) on kinked Au (16 14 15) substrate from DBBA precursor molecules. Surface reconstruction after growth is analysed by STM and electronic properties of 7-AGNRs by ARPES.

**Klíčová slova**
samousrporiadavané vrstvy, grafen, organo-kovové siete, TCNQ, BDA, molekuly
**Keywords**
self-assembly, graphene, metal-organic networks, TCNQ, BDA, molecules

KORMOŠ, L. *2D Molecular systems at surfaces.* Brno University of Technology, Faulty of Mechanical Engineering, 2020. 140 s. Thesis supervisor: doc. Ing. Jan Čechal, Ph.D.

CONTENTS

# 1. INTRODUCTION

For the past decade, the breakdown of the Moor's law [1], appears to be unavoidable. Although the downscaling of the devices continues with currently most advanced 7 nm node technology, the silicon-based transistors are reaching their limit. One indicator of the stagnation in the development of current conventional CMOS (complementary metal-oxide-semiconductor) transistors is a plateau in the progress of device frequencies that rarely exceeds 5 GHz. Combined with the increasing cost of downscaling in terms of fabrication and facility cost the drive to utilise new materials grows exceedingly in both scientific and industrial research groups. [2, 3]

In order to make significant improvements, several non-traditional materials and structures are considered in so-called *beyond-CMOS technologies*. Between them, a new branch of molecular electronics is being developed and already various molecular device has been discovered such as logic gates [4], diodes [5] or switches [6]. However, most recognised application of organic molecules today is OLED (organic light-emitting diode) displays, now widely utilised in the construction of TVs. OLED screens provide improved contrast, power efficiency and most notably, the flexibility that allows them to bend and even partially fold.

Several of the main prerequisites for the practical implementation of molecules as quantum bits were already fulfilled. First, the coherence time of MQBs was demonstrated in the range of hundreds of microseconds [7]. Second, dynamic control over the interaction between the individual metal centres in MQBs, for example, by employing photo-active or local electric control of a molecular linker [8]. Using chemical synthesis methods, two quantum bit gates have been implemented with atomic precision in one molecule. Additionally, the scalability of MQBs can be achieved by implementing principles of self-assembled and metal-coordinated long-range ordered molecular networks. For this and also many other applications, the understanding of the underlying principles of molecular self-assembly and interaction between the molecules and surfaces is of great importance.

Original full version of the thesis deals with a variety of surface-molecule systems ranging from weakly bonded self-assembled structures to metal-coordinated networks and eventually covalently bonded system achieved by on-surface synthesis. Thesis is divided into eight chapters beginning with introduction. Following second chapter provides theoretical overview focused on non-covalent bonds and various interactions most commonly involved in self-assembled processes of organic molecules on surfaces. Addi-

[1] empirical relationship stating that the number of transistors in integrated circuits will double about every two years [1]

tionally, several experimental examples are given for each relevant bonding mechanisms. Several sections of the review also include multiple examples of metal-coordinates systems with a last sections focused on graphene. Additionally, relevant introductions to a specific topics are given at the beginning of each experimental chapter.

The experimental results are presented in the last three chapters. Chapter five presents an extensive work focused on self-assembled structures of biphenyl-dicarboxylic acid (BDA) on Cu (1 0 0) and Ag (1 0 0). This molecule is model system due to its simple structure and the presence of carboxylic end groups that are often employed in the molecular self-assembly. In the first part of the chapter, the BDA/Cu (1 0 0) system is explored. The BDA on Cu chemically reacted (deprotonated) at room temperature and formed a single phase. On the contrary, the BDA on Ag (1 0 0) remains intact at RT. The deprotonation reaction on Ag was initiated by additional annealing, which lead to an abrupt change of binding mechanism of functional moieties and, consequently, to changes in the structure of the self-assembly. Variety of chemically and structurally distinct phases were observed and described in detail with the addition of main phase transitions followed in LEEM. In the last part of the chapter, the BDA on Ag (1 0 0) system is presented as the experimental realisation of long-range ordered uniform tessellations.

Chapter five describes the growth of high-quality graphene layers prepared on Ir (1 1 1) in UHV conditions. Graphene prepared in this way was utilised to study the self-assembly of BDA and TCNQ molecules. Graphene as a substrate for self-assembly has several advantages. It is a conductor with high electron mobility and a high spin diffusion length due to its negligible spin-orbit coupling [9]. Additionally, graphene is able to efficiently decouple the molecules from the underlying metal substrates due to its chemical inertness and low density of states around the Fermi level [10]. In this way molecules adsorbed on graphene can partially preserve their intrinsic properties such as magnetic moments or their catalytic activity [11, 12]. Further, controlled tuning of the charge carrier density in graphene devices may provide new opportunities to control the behaviour of molecular adsorbates [13]. On the other hand, molecules can be used as functionalising agents for graphene (or other 2D materials) based devices, that are also considered as one of the beyond CMOS technologies. Last sections of the chapter focus on the preparation of metal-coordinated molecular networks on graphene, mainly Fe-BDA and Ni-TCNQ.

# 2. MOLECULAR SELF ASSEMBLY

The engineering of materials with atomic or molecular-level precision requires high levels of sophistication in both fabrication and characterisation methods. A promising pathway lies in self-assembly of organic or metal-organic molecules on surfaces: a spontaneous formation of spatially textured networks of defined shape. Investigations focused on on-surface self-assembly started with the observation of self-assembled monolayers (SAMs). By exploiting non-covalent bonding between molecules it was possible to prepare large variety of self-assembled molecular systems on well-defined atomically flat surfaces. In the last couple of decades amount of research in this field rapidly grew, exploring systems prepared in ultrahigh vacuum (UHV) or at the liquid–solid interface with the ultimate goal of creating functional 2D systems. Molecules could be programmed to create an ordered structure tailored to desired function. [14–16]

Study of molecular structures on surfaces was greatly enhanced by the use of non-contact atomic force microscopy (nc-AFM) at low temperatures. Today, molecules can be observed individually with a sub-molecular resolution, and chemical reactions on surfaces can be observed step by step. Such imaging provides a valuable tool to investigate the intermolecular and molecule-substrate bonding mechanisms [17]. Surface confined molecular self-assembly mostly depends on (I) the mobility of the molecules on the surface, (II) the competition between intermolecular and molecule/substrate interactions and (III) the thermal energy brought into the system. The following sections focuses on non-covalent bonds and various interactions most commonly involved in self-assembled processes of organic molecules on surfaces.

## *2.1 Molecule - Molecule interactions*

A typical intermolecular potential can be conventionally described (or approximated) by Lennard-Jones potential ($A/R^{12} - B/R^{6}$), and the repulsive potential can be further improved by incorporating exponential function (Born-Mayer ($A \cdot e^{(-BR)}$) potential)[18]. In most cases, the potential will have a steep repulsive region at closer range and an attractive region at long range. At very short distances the repulsive forces will dominate the interaction arising from the Coulomb's energy, an increased nuclear repulsion as the ions are brought closer to each other by the bond formation. The other repulsive contribution is an increased electron exchange energy dictated by the Pauli exclusion principle. At long range, typically some energy minima exist where interaction between molecules becomes attractive. The most dominant attractive long-range effects are classical electrostatic attraction, forces between instantaneously formed dipoles,

and more complex dispersion forces [19].

### 2.1.1 van der Waals Interactions

The van der Waals force is generally used to describe weak long-range attractive interactions between atoms or molecules. However, its unambiguous classification is not possible. Van der Waals (vdW) interactions encompass attractive and repulsive forces over various distances 2 – 10 Å. The interactions usually have multiple contributions, mainly London force describing dispersion interaction and various dipole interactions between molecules with fixed or rotating dipoles depending on the interacting species. The interaction strength has a strong distance dependence and is often described (modelled) with term $1/R^6$ [20]. In self-assembly on surfaces, the van der Waals interactions can be the main driving force (together with surface interactions) for larger and otherwise non-interacting molecules [21].

#### *Dispersion interaction*

Part of vdW forces are dispersive interactions, which play an important role in the formation of self-assembled structures often in combination with other bonding mechanisms between the molecules or molecules and surface [22]. Dispersion interaction has a quantum-mechanical origin and is more dominant at the long-range. This interaction between the atoms/molecules is formed due to a correlation between the motion of their electrons, and this manifests itself in such a way that lower-energy configurations are favoured and higher-energy ones disfavoured. The average effect is a energy decrease, and since the correlation effect becomes stronger as the molecules approach each other, the result is an attraction (up to a certain distance until other interactions prevail). In literature, this interaction is sometimes refereed to as London forces, charge-fluctuation forces, electrodynamic forces or induced-dipole–induced-dipole forces. Dispersion interaction needs to be considered in density-functional theory (DFT) calculations of larger systems such as self-assembled layers, to provide accurate results [23]. The general features of dispersion forces can be summarised as follows [20]:

1. They are long-range forces and can be effective from large distances (> 100 Å) down to interatomic spacings (about 2 Å).

2. They may be repulsive or attractive, and in general, dispersion forces between two molecules or large particles do not follow a simple power law.

3. Dispersion forces not only bring molecules together but also tend to align or orient them mutually.

4. Dispersion forces are not additive; that is, the force between two bodies is affected by the presence of other bodies nearby (nonadditivity).

### 2.1.2 Hydrogen bonds

Hydrogen bonding is the most frequently observed non-covalent bonding [24]. It can be found in various disciplines from biology (DNA base pairs bonding [25]) to crystallography [26]. Hydrogen bonds are often involved in self-assembly due to their reversibility, selectivity, directionality and relative strength. However, the exact nature of the hydrogen bond is still a matter o scientific discussion. According to the International Union of Pure and Applied Chemistry (IUPAC) recommendation from 2011, the hydrogen bond $X-H\cdots Y$ is defined as: "...an attractive interaction between a hydrogen atom (H) from a molecule or a molecular fragment X-H in which X is more electronegative than H, and an atom or a group of atoms Y in the same or a different molecule, in which there is evidence of bond formation. " [27].

### 2.1.3 Halogen bonds

Another type of a non-covalent bond is the halogen bond formed between the electrophilic region of halogen atom ($\sigma$-hole) in a molecule and a nucleophilic region in another or the same molecule. This bond can be denoted as $R-X\multimap Y$, where X is the halogen atom covalently bonded to the R group and having the electrophilic region, and Y is a donor. The Y species can be an anion or a neutral group possessing at least one nucleophilic region, e.g., a lone-pair-possessing atom or $\pi$-system. However, the exact nature of the halogen bond cannot be fully explained only by the $\sigma$-hole model. The secondary region of a negative potential forms around the $\sigma$-hole and can interact with the electrophilic species.

In self-assembly, the halogen bond can be viewed as an alternative to the hydrogen bond because it has similar properties. However, halogen bonds have higher directionality that can drive self-assembly process. This directionality arises as a consequence of the $\sigma$-hole localisation, i.e. opposite to the covalent bond(s) that the halogen atom is bonded to.

### 2.1.4 Intermolecular $\pi$-$\pi$ interaction

The interaction between two aromatic molecules can generate sufficient force to influence self-assembly between $\pi$-rich molecules. The electrostatic model can explain the origin of this interaction. However, a detailed understanding of the nature and properties of $\pi$-$\pi$ is not available yet. A simple model of the charge distribution was presented by Hunter and Sanders, which accounts for many of the experimental observations [28]. The model considers the aromatic molecule as a set of three charges, one positive (+1) sandwiched between two negative ones (-0.5). In this configuration, direct staking is disfavoured as two negative charges directly next to each other are repulsed. Optimal $\pi$-$\pi$ interaction of two molecules will then favour $T$ shaped structure or displaced stacking structure where the $\pi$-rings are shifted towards each other [29]. Interaction between aromatic molecules plays an important role in some chemical

reactions and protein recognition [30].

### 2.1.5 Electrostatic interaction

Molecules exhibiting permanent charges, dipoles or quadrupoles, will generate electrostatic fields that will interact and can affect self-assembly process. Electrostatic interaction can be divided into multiple groups. The most straight forward one, is the ionic bond that form between two molecules or atoms of different types, one with positive (cation) and one with negative (anion) charge. A special type of molecules that appear neutral, but have both positive and negative charges at a separate positions are called zwitterions. An example of such a molecule is an amino acid *L*-methionine. Methionine can self-assemble on Ag (1 1 1) in molecular chains and form unique nanogratings of various periodicity [31].

In the case of molecules with a permanent dipole, the interaction is generally weak and depends on the mutual orientation of the molecules. In the cases when dipoles can be approximated by the classical dipole, interaction strength scale with the distance approx. $1/r^3$. Several self-assembled structures have been reported to be stabilised by dipolar interactions. One example is the hexaaza-triphenylene-hexacarbonitrile (HATCN) molecule on the surface of Au (1 1 1) [32]. The report has shown that HATCN molecules form linear and hexagonal porous structures.

## 2.2 Molecule-surface interactions

The second most influential force in self-assembly is the interaction between molecules and surface. Adsorption of molecules is most commonly classified as either weaker physisorption or stronger chemisorption. The term chemisorption usually implies the presence of a bond between the surface and adsorbed molecule. In the case of physisorption, van der Waals forces are often claimed to be the only interaction causing the phenomena. However, here there is some confusion in literature because today, the wan der Waals forces are not clearly defined and encompass a variety of interactions as mentioned above. To generalise, there are specific properties that differentiate the physi- and chemi-sorption; however, there is no sharp distinction between them. For example, hydrogen bonding can be considered as an intermediate case because it involves various interactions and can have different strengths.

### 2.2.1 Metal-organic interface

The most common surfaces used for examining self-assembly of organic molecules are noble metals and graphite (HOPG; that is more often used for liquid/solid interface). Their advantage lies in the low reactivity that allows molecules to move and assemble, and their high conductivity allows a straightforward access by surface science techniques (e.g., STM, XPS).

The electronic structure at the interface of the molecular layer and metal can involve multiple effects such as the energy level alignment, band bending, charge transfer and the formation of new interface states. Current models describe formation of a dipole layer at the interface of most M/O systems. Various theories are used to describe dipole formation in differently interacting systems.

In the category of chemisorbed molecules, charge can be transferred from the metal to the molecule, e.g. TCNQ/Au or vice-versa in case of methylphenyl-biphenyl-diamine (TDP) on Au. This charge redistribution results in the formation of an interfacial dipole [33]. Similarly, the dipole can form due to the strong bonding between the molecule and metal. Additionally, the substrate can also affect a charge transfer between different molecules in donor-acceptor systems.

In the case of physisorbed molecules, two phenomena are most prominent, the pillow effect and image charge effect. The image charge effect can be described as the formation of a weak dipole in the molecule due to quantum oscillations, followed by an image dipole formed on the metal surface. The interaction of these dipoles gives rise to van der Waals force between the molecule and metal. The origin of the pillow effect lies in another quantum mechanical effect, the Pauli exclusion principle.

### *2.2.2 Metal-organic systems*

The deposition of reactive metals on a non-reactive substrate can direct the formation of new assemblies. The bonding between organic molecules and metals is typically stronger than the substrate-molecule interaction. Two bonding mechanisms are usually utilized in growth of metal-organic networks, electrostatic (ionic) bond and metal-coordination (dative) bond. Metal coordination networks sometimes incorporate atoms that are provided by the substrate itself.

Coordination networks on surfaces are named after their 3D analogue in solution chemistry. Coordination bonding is a type of covalent bonding formed by two atoms sharing a pair of electrons, where both electrons are provided by one of the atoms. This electron pair is then attracted to both atomic nuclei and holds the atoms together. Coordination compounds can form a large variety of regular porous structures with tailor made size and chemical properties, which made them an exciting research topic. Coordination networks on surfaces have been synthesised by a variety of metal adatoms (Co, Cu, Fe, Cr, Mn, Ni) and molecular binding groups (hydroxyls, carboxyls, cyano or pyridine groups) [16, 34].

The surface is not only a tool to crate structure with a planar geometry. In solution, a coordination bonding is usually formed by metal cations with known oxidation state (positive or zero). However, metallic surfaces provide a reservoir of electrons for coordination atoms allowing them to donate (or possibly accept) charge without becoming charged themselves [35]. Therefore, the nature of the bond can differ from the well understood liquid phase counterpart.

# 3. BIPHENYL DICARBOXYLIC ACID ON METAL SURFACES

The biphenyl-dicarboxylic acid (BDA) networks were used as a model system to study supramolecular chemistry and self-assembly. The BDA molecule, as shown in Fig. 3.1(a), is formed by two phenyl rings that are symmetrically functionalised by carboxylic end groups. Molecules with carboxylic groups have been extensively studied with a focus on their surface self-assembly. Especially the di- and tri-carboxylic acids were researched on a variety of metal surfaces including Cu [36–39], Ag [40, 41], Au [42, 43], and Pd [44]. The intact DBA molecule usually maintains a flat adsorption geometry on metals, and it is stabilised on the surface via complementary hydrogen bonding between carboxyl groups and additionally by the van der Waals interactions bringing BDA sides closer together [45]. In this way, carboxylic acids build up a variety of structures often formed by long molecular chains both separate or adjacent to each other [36–38, 40].

Exploring the BDA interactions with surfaces can improve our general understanding of the carboxylic group's role during the self-assembly process and surface reactions. That, in turn, will allow to design and fabricate improved supramolecular nanostructures with well-defined properties.

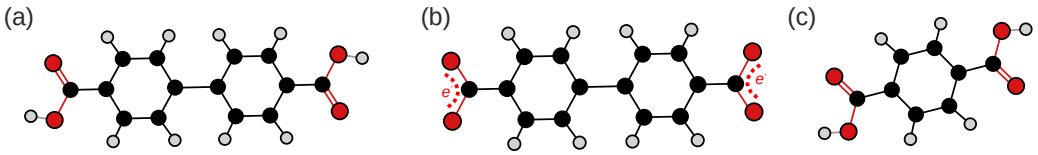


*Fig. 3.1:* (a) Chemical Structure of 4,4-Biphenyl Dicarboxylic Acid (BDA), (b) deprotonated BDA and (c) Terephthalic acid (TPA).

## *3.1 BDA on Cu (1 0 0)*

On the surface of copper, the BDA deprotonates: hydrogen is removed, and resulting carboxylate groups bind to the copper surface. The exact mechanism of BDA-Cu interaction was the object of some discussion in the literature. Original studies of similar terephthalic acid (TPA) on Cu (1 0 0) suggested that molecular assembly is a result of the interplay between molecule-substrate interaction and intermolecular hydrogen bonding [36, 46, 47]. However, later studies reported that molecular deprotonation takes place near room temperature, and strong oxygen copper bonds will dominate the molecular self-assembly.

On the surface of Cu (1 0 0) at the room temperature, only a single BDA phase was observed consisting of fully deprotonated molecules. The structure of this phase is

shown in Fig. 3.2, together with the proposed model consistent from both LEED and STM data. The LEED pattern taken over a large number of BDA islands shown in Fig. 3.2(a) can be associated with $(4\sqrt{2} \times 4\sqrt{2})$R45°, or equivalently, $c(8 \times 8)$ molecular superstructure. Single BDA molecule appears as symmetric rod-like protrusion with the apparent length of $1.08 \pm 0.03$ nm (measured at 10 % of the maximum height). This length is comparable with a theoretical length of 1.14 nm obtained by gas-phase geometry calculation using Arguslab and considered in recent studies [46, 48]. In the high-resolution STM image in Fig.3.2(b), a long-range ordered structure of the self-assembled BDA can be observed. Islands typically extend in range of 30-100 nm depending on the terrace size, at the submonolayer BDA coverage of approx. 0.4 – 0.6 ML. Within the molecular domain, the adjacent BDA molecules are oriented perpendicular to each other; the carboxylate moiety of each pointing to the centre of the neighbouring BDA.

Based on the available data structural model shown in Fig. 3.2(c) was created. It presents binding motif where two carboxylate oxygen atoms point to two distinct substrate atoms and phenyl rings are localised near substrate hollow sites. Relative positions of BDA on Cu (1 0 0) were determined following recent studies [46, 49]. The model suggests that substrate mediated molecular interaction will be the dominating factor in the self-assembly.

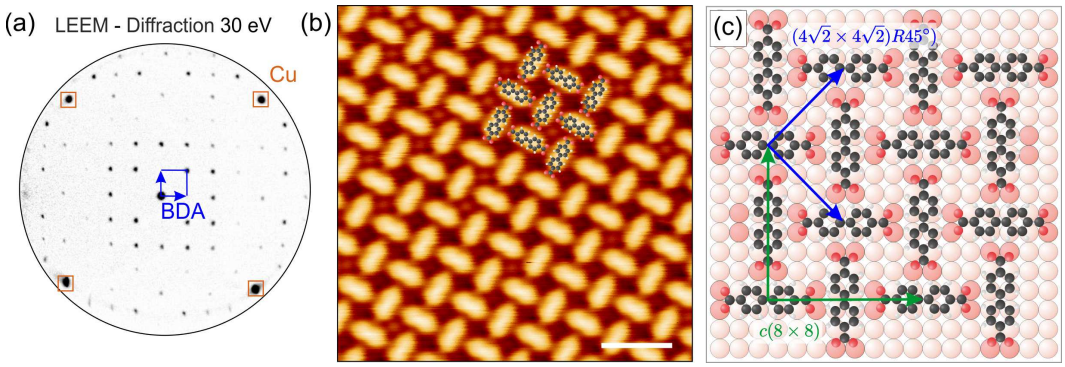


*Fig. 3.2:* (a) LEEM image measured at 30 eV. Cu (1 0 0) diffraction spots are marked in orange and BDA molecular superstructure in blue. (b) STM image of BDA molecular self assembled structure on Cu (1 0 0) surface with superimposed molecular model. Scale bar is 2 nm. (c) Model of the proposed BDA phase.

A significant charge transfer from the BDA carboxylate group to the substrate was observed previously [50]. Additionally, strong bonding between the O atoms in carboxylates in TPA and the Cu atoms caused buckling of the first Cu layer [51], similarly to the above-mentioned case of TCNQ. Carboxylates in this case displayed strong carboxylate oxygen binding to substrate, charge transfer, and lifting of substrate atoms. On this basis, it can be assumed that a single substrate atom cannot accommodate the binding of two and more carboxylate oxygen atoms. In any case, the proposed model dictates that two carboxylate oxygen atoms point to two distinct substrate atoms (site exclusion model).

### 3.1.1 Growth Anomalies of BDA on Cu (1 0 0)

Extended decoration of the step edges was observed for the vast majority of inorganic systems where monomers are single atoms displaying isotropic behaviour [52]. Additionally, many organic systems also nucleate on the step edges [53, 54]. Growth of BDA islands on the Cu (1 0 0) is one example where molecular island growth differs from typical systems. Observations in LEEM found no preference for nucleation at atomic step edges consistent with the previous work [55, 49]. This behaviour makes the presented system important from both a fundamental and application point of view. In the real space LEEM image in Fig. 3.3(a), one can observe that BDA molecule form separated islands. The BDA molecular islands appear as dark contrast areas, and the Cu substrate appears bright and upon closer inspection lines representing step edges and narrow terraces can be observed. Further, large area STM image in Fig. 3.3(b) confirmed that molecular islands are distributed over the terraces and touching the step edges only in few points. The origin of strong non-wetting of the step edge was not previously identified despite multiple studies of systems comprising BDA [37, 46], or similar TPA[51, 56], and other related dicarboxylic acids [41] on Cu substrates. This originally promoted further studies into this system.

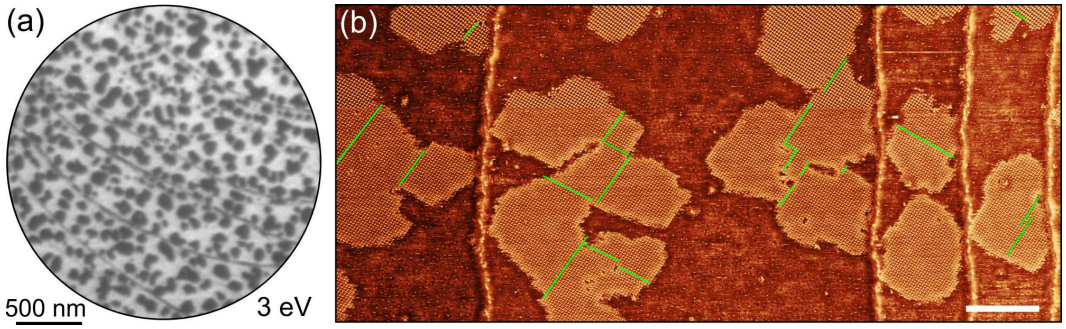


*Fig. 3.3:* Self-assembled islands of BDA on the Cu (1 0 0) surface: (a) LEEM image measured at 3 eV. Dark areas correspond to the molecular island and light gray to the substrate. (b) Overview STM image on the same sample. Green lines mark line defects in the molecular assembly, separating different molecular islands. STM image contrast was enhanced by adaptive filtering. Scale bar is 25 nm.

### 3.1.2 Step edge passivation

Previous sections argued strong molecule-atom interaction between the BDA and Cu, and, therefore, one can expect even stronger step edge interaction, which appear incompatible with the idea of BDA non-wetting the atomic step edges. In fact, closer look on the step edges of Cu(1 0 0) revealed a dense decoration by BDA molecules as shown in the STM images Fig. 3.4(d-e). Molecules at the steps are preferentially oriented in the same direction ⟨1 0 0⟩ or rotated by 45° with the respect to the BDA orientation in the islands ⟨1 1 0⟩. Given the high step-edge reactivity, some additional structures could be observed that are ascribed to the molecular fragment or other contaminants

on the surface. These structures provide anchoring sites for molecular domain attachment as previously shown in the STM image in Fig. 3.3(b). However, the majority of the molecules attached to the steps retain features consistent with the appearance of intact BDA molecules.

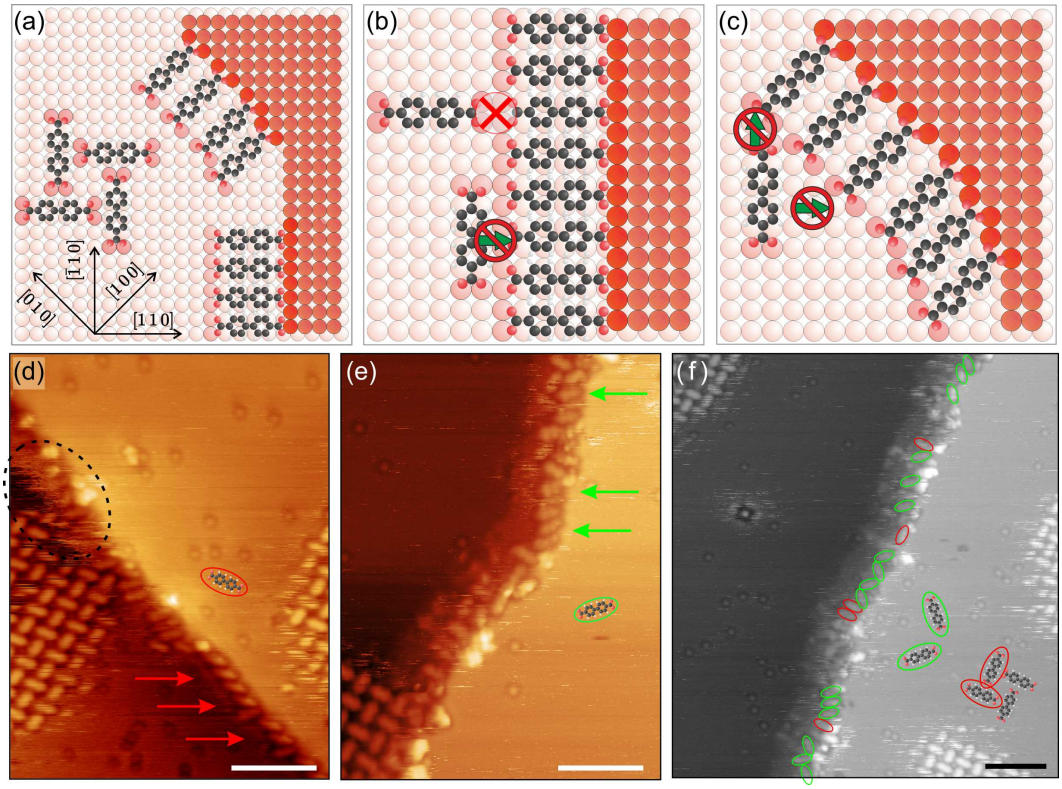


*Fig. 3.4:* (a-c) Models of the BDA molecules bonding to the Cu (1 0 0) atomic steps edges. Majority of the molecules at the steps are rotated by 45° with respect to the BDA orientation in the islands. Diffusion of molecules along and over the step edge is limited. (d-f) Detailed STM images of BDA step edge decoration. Molecules in the direction of the islands are marked in red and rotated molecules in green. (d) Increased noise in the STM encircled in black suggests trapped molecules between the island and the step edge since they cannot attach or diffuse to the next terrace. Scale bar is 4 nm.

By careful examination, several high-resolution STM images from multiple experiments were selected for statistical analysis. As shown in one of the selected images in Fig. 3.4(f), the orientation of the BDA was determined from the self-assembled phase. Molecules at the step edges were identified and were assigned the orientation. Only the molecules that can be unambiguously identified were included. Over 200 molecules were counted for which the ⟨1 0 0⟩ direction (molecules rotated in respect to the self-assembled phase) was slightly favoured over the ⟨1 1 0⟩ one, with the ratio of 1.6 : 1. These orientations are in accordance with the previously presented tentative model, as shown in Fig. 3.4(a-c).

The dense molecular packing of BDA at the step edges prevents the attachment of additional BDA molecules and hinders the formation of extended molecular islands.

Some molecular islands were attached in areas without the decoration by intact BDA. The area between the BDA islands and the step edges often exhibited high noise levels in the STM, even when the other features appeared in high resolution. This implies high mobility of the BDA molecules in these areas and suggests another possible aspect of the BDA passivated step edge: the formation of a barrier against the diffusion of BDA molecules across the step edges (a type of Ehrlich-Schwoebel barrier). The molecules trapped between the BDA islands and step can neither attach to the passivated steps nor diffuse to the next atomic terrace.

## 3.2 BDA on Ag(100)

The following section describes the step by step deprotonation of BDA on the Ag(100) surface. Multiple structural assemblies (phases) of BDA are presented, corresponding to fully- and partially protonated molecules as well as deprotonated molecules. Additionally, at specific conditions a mixture of fully-, partially- and non-deprotonated BDA coexists on a substrate. Hence, we can view this system as the multi-component assembly of structurally close but chemically distinct molecular building blocks.

### 3.2.1 Overview

Combination of the mesoscale viewing area of LEEM, nanoscopic details from STM and chemical information from the XPS revealed multi-step deprotonation process of BDA on the Ag(100). During the continuous annealing of BDA/Ag(100), several phases consisting of BDA molecules with a distinct level of deprotonation were identified: fully protonated (2H-BDA), semi-deprotonated (1H-BDA), and fully deprotonated (0H-BDA). Main molecular phases shown in Fig. 3.5 are denoted as α-phase: a fully protonated molecules (as deposited); β-phase: formed by partially deprotonated BDA; γ-phase: a mixture of partially and fully deprotonated molecules and δ-phase: fully deprotonated phase of BDA. Each phase will be described in detail in the following section. In addition, multiple intermediate phases and phase transformations observed in LEEM will be shown.

The BDA molecules were deposited onto an Ag(100) crystal held at the room temperature. After the transfer to the LEEM chamber, the sample was analyzed and slowly heated by the filament (IR-heating only). The increased temperature initiated the deprotonation process and associated phase transformation. Changes of the molecular island were carefully observed in the LEEM, and the transformation was stopped at specific points. The sample was then cooled down to the room temperature and analyzed. By utilizing μ-diffraction aperture every structural domain of the BDA was identified. Each phase consisted of multiple equivalent molecular domains, and experiments sometimes yielded mixtures of different phases. After the transformation and LEEM analysis in the LEEM were finished, the sample was transferred to the STM or XPS chamber for further measurements. Numerous experiments were performed with

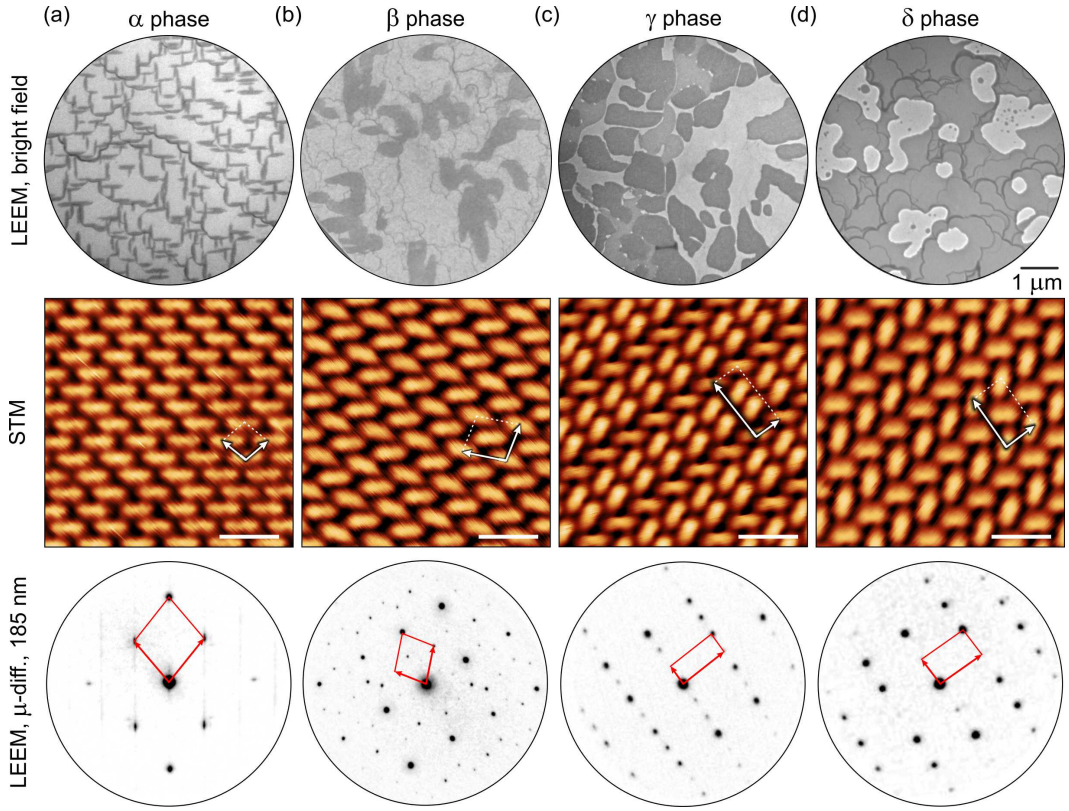


*Fig. 3.5:* Change of BDA molecular phases on the surface of Ag (1 0 0) with increased temperature. (a-d) Each phase represent the different chemical composition of BDA and is stable after the cooldown of the sample to the room temperature. LEEM images represent the typical appearance of molecular islands of different phases. Images were acquired at 10 eV with inserted contrast aperture. Corresponding STM images are in the second row. Diffraction patterns in the last row represent a single molecular island (domain) on the surface and were acquired by inserting µ-diffraction aperture (diameter of 185 nm). The unit cells of molecular superstructures are marked by a red in diffraction patterns and white in the STM images. Scale bars in STM images are 2 nm.

several silver crystals and yielded consistently the same molecular phases. Molecular layers were also transformed in several vacuum chambers and also in another laboratory (for nc-AFM measurement).

### *3.2.2 XPS analysis*

Distinct chemical composition of each BDA phase was identified in-situ, by X-ray photoemission spectroscopy. Conventional non-monochromatic X-ray source that utilized Mg K α radiation with 300 W emission power and 12.5 kV cathode-anode voltage was used for all measurements. The C 1s and O 1s detailed spectra were acquired in high magnification mode using pass energy 20 eV integrating up to 180 sweeps with 0.1 s dwell time and 0.05 eV energy step. Normal emission geometry (emission angle 0°) was employed. The prolonged measurement time was necessary due to the weaker oxygen signal for sub-monolayer BDA coverage.

First, the reference spectra of BDA was measured from a multilayer, shown in the first row of the Fig. 3.6. Here, it was assumed that any surface effect of the Ag substrate would be negligible in overall data. The detailed spectra of C 1s were fitted by three components and simultaneously adjusted Shirley background. The largest component of the multilayer BDA carbon can be associated with the carbon atoms of phenyl ring (C1, blue) at the binding energy of 285.4 eV and the second component with the carbon bound to a carboxyl group (C2, red). The third component (C3, green) was attributed to the shake-up satellite due to $\pi - \pi^*$ transition in the aromatic ring.

Spectra of submonolayer coverage of intact BDA (α-phase) exhibited two main differences compared to the multilayer. First, an additional forth carbon component (C4, magenta) was added to properly fit the C 1s spectra. This component was shifted by 1 eV towards higher binding energies and could be associated with the carbon atoms that are detached from the surface. Such effect may occur for either a BDA molecule moving in the molecular gas or part of the BDA that is lifted from the surface due to the compression in the self-assembled structure. Some hight variation was observed in the nc-AFM data, and this will be introduced appropriately later (Fig. 3.10). Alternatively, this peak could be explained as a signal from adsorbed CO molecules or by an asymmetry in the C1 carbon component. The second difference is that the main C1 component is shifted by ~ 0.5 eV toward lower binding energy. The corresponding shift can be observed for O 1s peak. Similar shifts are often explained for adsorbed molecules as a screening of the core levels by metal substrate, i.e.: effect of the charge transfer from the substrate to the adsorbate [57]. The peak positions are in agreement with the previous studies of carboxylic compounds [58, 59]. The intensity ratio of peaks associated with carboxylic and phenyl carbon atoms is 0.16, that is in agreement with the expected ratio of 2:12 (0.167) for BDA molecule.

The O 1s peak of multilayer BDA was fitted by two components corresponding to the two distinct oxygen atoms in the carboxylic group. The background was changed to a combined Shirley-linear model. The linear component was included to compensate for a decreasing background intensity at the high binding energy side of Ag 3d peak. The intensity of oxygen components is close to 1:1, which is in agreement with the presence of intact carboxylic groups. The spectrum of the α-phase is qualitatively consistent with the multilayer except for the rigid shift, also observed for the C 1s peak and described above.

Understanding the XPS spectrum for the intermediate β- and γ-phases presented a substantial challenge. Original hypothesis follows the idea of typical chemical reaction: by annealing, the BDA molecule will undergo deprotonation process. The experiment should yield either protonated or deprotonated BDA molecules with the possibility of a mixed compound of both if the chemical transformation was not completed. The oxygen XPS spectrum was expected to be composed of 3 components, the hydroxyl oxygen (O1) and carbonyl oxygen (O2) of the carbonyl group and carboxylate oxygen atoms (O3) of deprotonated BDA (a reminder of the nomenclature is in Fig. 3.7). This follows the previous studies of the terephthalic acid on Cu (0 0 1) [51, 39] and Ag [36].

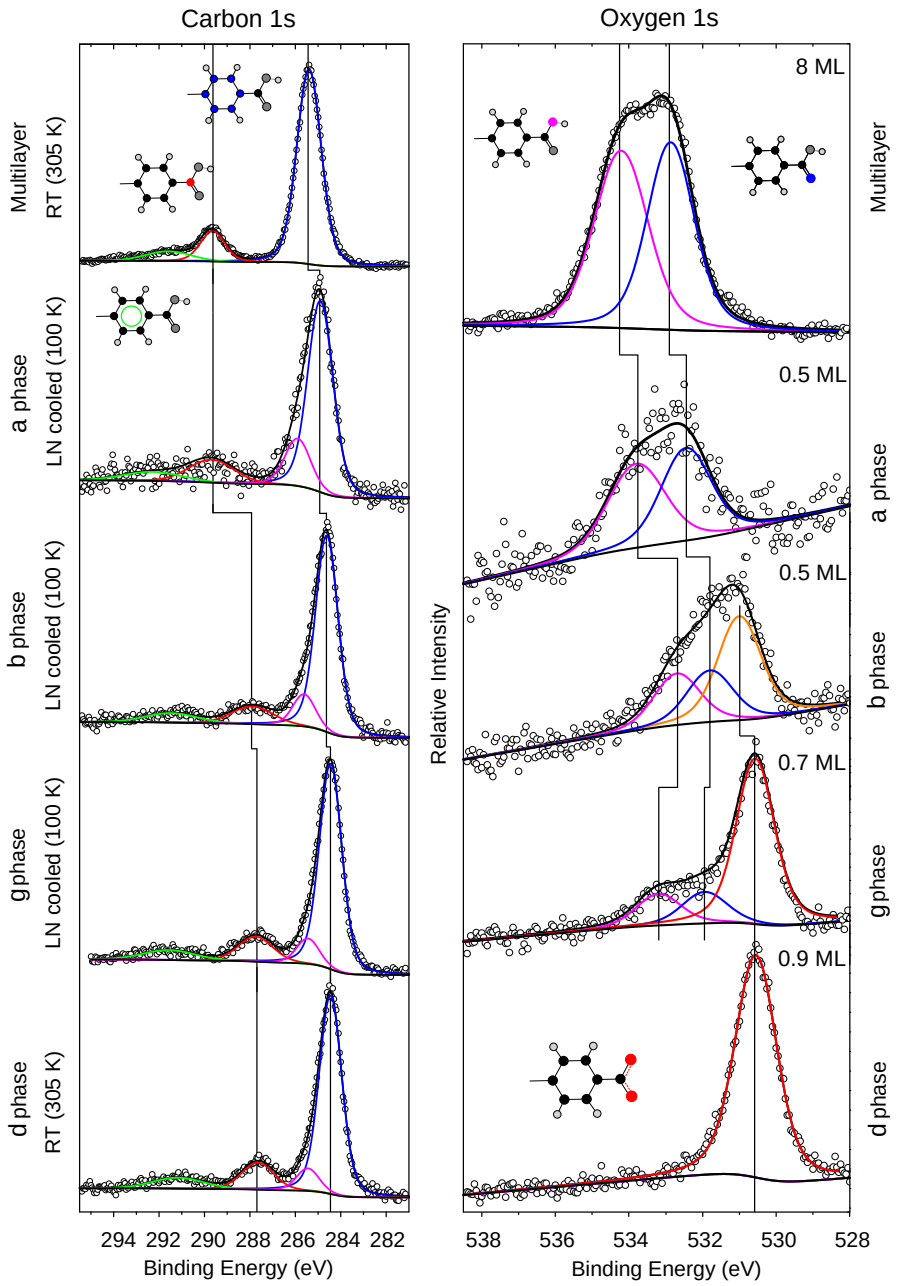


*Fig. 3.6:* Detailed photoemission spectra of C 1s (left) and O 1s (right) peaks measured for all main BDA phases on Ag (1 0 0). Additionally, reference spectrum from BDA multilayer (~ 8 ML) is included in the first row. The thickness of the BDA layer and temperature of measurement is marked in the respective graphs. Coloured atoms in the molecular schematic indicate the corresponding peak in the spectra.

Indeed, the new oxygen component is present in the β- and γ-phases spectra as was expected due to the presence of new deprotonated molecules on the surface. Additionally, the carbon C4 component was shifted to lower binding energy by ~ 1.8 eV confirming the expected chemical change. However, the oxygen spectrum is significantly shifted compared to the α-phase. Further, the position of the new oxygen component is also shifted compared to the fully deprotonated phase of the BDA. Quiroga et al.

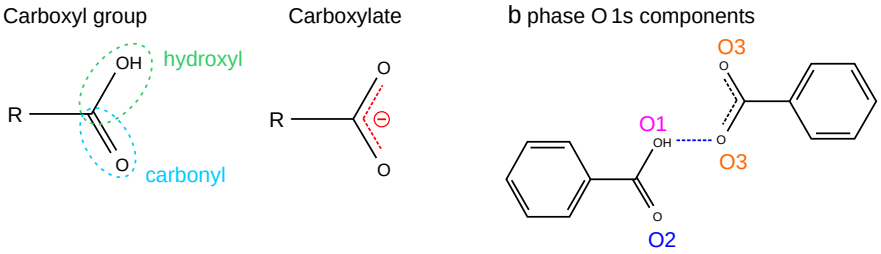


*Fig. 3.7:* Chemical scheme of the carboxyl and carboxylate groups. Binding configuration of β-phase (right), intact carboxyl group forms hydrogend bond with carboxylate. The spectral components of O 1s peak are marked as O1, O2, and O3 next to the associated hydroxyl, carbonyl and carboxylate oxygen atoms, respectively.

[39] explored in detail the similar changes in case of the terephthalic acid on Cu (0 0 1). Substantiated by DFT theoretical calculations, they explained that the shifts are a result of the hydrogen bonding environment between partially and fully deprotonated molecules.

Proposed bonding scheme for the BDA β-phase is shown in Fig. 3.7. Deprotonated carboxylate oxygen was assigned to the O3 fitting component at the energy of 531 eV, in agreement with the reported peak component for TPA/Cu [39]. Component O1 was assigned to hydroxyl oxygen) bonded trough hydrogen bond to carboxylate oxygen. Its energy position 532.7 eV is close to reported 532.5 eV [51, 39] and the energy shift from the alpha phase −1.1 eV is comparable with reported value −0.9 eV. Position of the O2 component 531.8 eV is higher than 531.1 eV reported for TPA/Cu. However, the energy shift of the C2 component of 0.7 eV is much closer to the reported value of 1.0 eV. The discrepancy in the peak shifts is possibly caused by different charge transfer between carboxylate and Ag surface compared to the Cu. The ratio of the O1:O2:O3 peak area of the components is 1:1:2, which means the ratio of protonated and deprotonated carboxylic groups is 1:1. This ratio can be explained by either an 1:1 mixture of fully deprotonated and protonated molecules or only partially deprotonated BDA molecules.

In next spectrum of the partially deprotonated BDA γ-phase the O1 and O2 components of the oxygen peak associated with hydroxyl and carbonyl peaks shift back to the higher binding energy. Importantly, the energy separation of these components returned to the value of 1.25 eV (from 0.9 eV in β-phase). This energy is close to 1.35 eV that was observed for the α-phase. Finally, the interpretation of the spectrum of the fully deprotonated δ-phase of BDA was straightforward. The O 1s can be fitted with the single component, associated with carboxylate oxygen, at 530.7 eV, which is in agreement with similar systems [59]. No energy shift compared to the γ-phase was observed. A single component is consistent with the symmetric binding environment of both carboxylate oxygen atoms.

### 3.2.3 Strucure of the BDA α-phase

The intact BDA α-phase deposited on the Ag surface at room temperature grows in small islands in almost a needle-like fashion. The molecular islands appear to be preferentially growing out of the substrate steps edges indicating that the step edges present preferential nucleation sites and are not passivated by BDA, contrary to the Cu (0 0 1) described in the previous section. Elongated BDA islands preferentially grow in the substrate high symmetry orientations ⟨1 1 0⟩. The μ-diffraction images in Fig. 3.8(b), taken from individual islands, show that there are two rotational domains of the self-assembled BDA. Further, the dark field LEEM images were acquired for both molecular domains, and their superposition over the bright field image confirmed that they include all of the molecular islands on the surface as shown in Fig. 3.8(d).

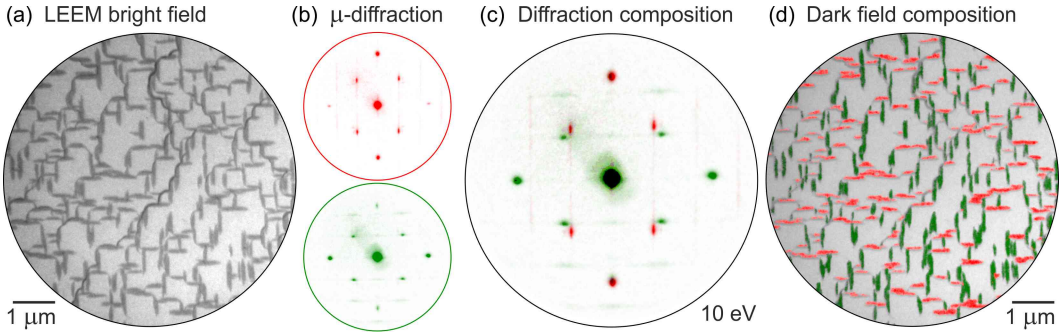


*Fig. 3.8:* LEEM data of α-phase: (a) Bright field LEEM image where molecular islands appear as a dark features. (b) The μ-diffraction acquired from individual BDA islands. (c) Large area diffraction image overlay with the μ-diffraction images. (d) Dark field images acquired from individual BDA structural domains superimposed on top of the bright field image (a).

The STM measurement revealed a well ordered self-assembled structure of the BDA shown in the overview Fig. 3.5(a) and in more detail in Fig. 3.9. Here, the STM image was aligned based on the previously measured atomic resolution images of clean Ag (1 0 0) surfaces. This was reasonable approximation because the position of the crystal in the sample holder was fixed over time. Molecules formed a closely packed structure of straight molecular chains with an inter-chain distance of 5.5 ± 0.3 Å. Chains packing exhibits regular periodicity that can also be observed as prominent spots in the μ-diffraction images in Fig. 3.8(b). On the contrary, in the direction of the chains, the spacing of the molecules was variable. This can be observed in the STM image overlaid by a periodic lattice in Fig. 3.9.

Considering the shape of the BDA molecules and XPS chemical information that confirmed their intact chemical state, the BDA molecules were assumed to be arranged in head to head fashion. This assembly is stabilized by electrostatic hydrogen bonding between opposing carboxylic groups in agreements with multiple studies were the hydrogen bond was suggested as a driving force of the BDA self-assembly. The variation in the molecular distances corresponded to alternating intermolecular bonds that are in the range of 2.4 – 3.3 Å. The bond length was calculated from theoretical BDA

length of 11.4 Å (length from O to O along the molecule) subtracted from measured molecule-molecule distances in STM images. Alternating molecular distances suggests that substrate-molecule interaction will play a significant role in the BDA self-assembly on Ag(1 0 0).

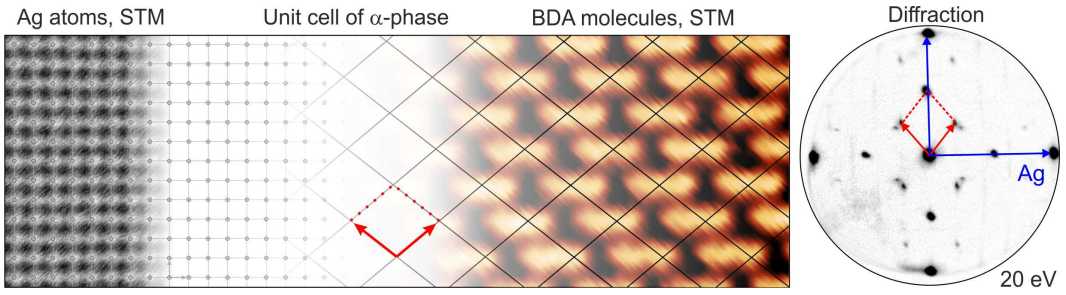


*Fig. 3.9:* STM data: composition of the atomic scale images of Ag (1 0 0) surface with the deposited BDA α-phase and large area (~ 300 µm$^2$) diffraction pattern acquired at 20 eV.

A low temperature STM/AFM measurement shown in Fig. 3.10, was performed on the BDA α-phase. The measurement utilized a qPlus sensor functionalized by a CO molecule in a commercial CreaTec UHV system [17]. Detail of the self-assembly from STM shows prominent features that appear to be connecting the molecular chains. However, the nc-AFM measurement that reflects the actual hight profile of the molecules revealed that these features are formed by non-planar adsorption of the BDA. The two phenyl rings of the molecule are mutually twisted, as shown in Fig. 3.10(b). Additionally, the bright spots are observable between the BDA carboxylic oxygen sites that are a signature of complementary hydrogen intermolecular bonding [60].

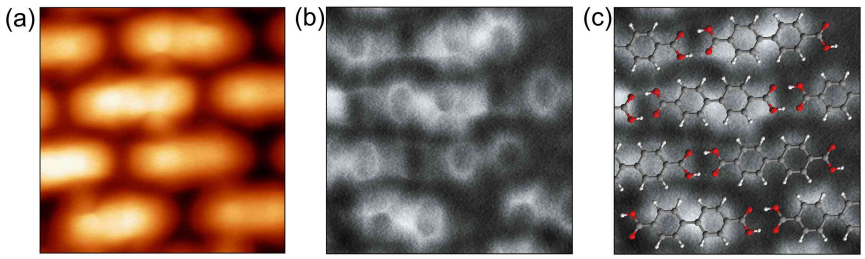


*Fig. 3.10:* Low temperature measurement: (a) Detail of the BDA α-phase in STM measured at 5 K. (b) nc-AFM image of the same area measured with qPlus sensor functionalized by CO molecule. (c) nc-AFM with model of the BDA molecules.

Based on the available data: STM, nc-AFM, diffraction pattern and simulating the diffraction spots in the *LEEDpat* [61], the following model was created. Each chain of the BDA molecules lays over two Ag atoms in the ⟨1 0 0⟩ directions of the Ag (0 0 1) surface. Both oxygen atoms are located near the on-top sites at similar heights, and the lateral repulsion of the molecular arrangement twists the phenyl rings of the BDA molecules differently as seen in the AFM data. The α-phase unit cell most closely approaches $\begin{pmatrix} 2 & -2 \\ 2 & 14/5 \end{pmatrix}$. Hydrogen bond length corresponding to this unit cell can be

calculated 0.245 Å, which corresponds to the measured minimal lengths from STM images (strongest hydrogen bond). However, hydrogen-bonded pair of BDA at the optimal position is incommensurate with the substrate periodicity.

The mutual distance between two BDA molecules is governed by BDA-BDA optimal hydrogen bonding length, but the BDA-substrate interaction is maximal for the optimal position of BDA in respect to substrate atoms. Hence, with every new BDA in a chain, the BDA-substrate shift is increased. Once it surpasses the hydrogen bond energy, it will become more energetically favourable to break the hydrogen bond and align the BDA position with respect to the substrate. The resulting irregular intermolecular spacing caused by competing BDA-BDA and BDA-substrate interactions can be observed as tear in the self-assembly.

### *3.2.4 Structure of the BDA β-phase*

The formation of the DBA β-phase was thermally induced by annealing to approx. 70 °C. The new phase consist of larger molecular islands, compared to the α-phase, as shown in Fig. 3.11(d). The diffraction image taken from the displayed area is formed by a combination of four rotational domains of the β-phase. Each domain is shown in Fig. 3.11(c) and was measured from individual islands acquired by μ-diffraction aperture in the LEEM. Observation of four rotational orientations is consistent with unit cell rotation in respect to principal substrate directions and the fourfold substrate symmetry. Additionally, individual islands of corresponding rotations were visualized with dark-field imaging, and the coloured composition image is displayed in Fig. 3.11(e). All of the domains were homogeneously distributed on the Ag surface. The unit cell of β-phase contains four BDA molecules and exhibits the interlocked row structure as can be observed in the STM Fig. 3.11(a).

### *3.2.5 α ⇒ β phase transformation*

The real-time observation of the structural transition between the BDA phases was possible thanks to the fast image acquisition in the LEEM. The sample was heated at a rate of approx. 1 – 3 °C/minute. During the transformation, the bright-field images were recorded every 1 s and the thermal drift of the sample was corrected later in the data processing. In the initial moments of heating the α-phase islands undergo significant morphological changes without change of the self-assembly structure. Some of the smaller BDA islands decrease in size, and simultaneously other islands grow. This phenomenon is known as Ostwald ripening. The BDA molecules are moving between the island in the state of 2D gas, available on the surface. Progress of α ⇒ β transformation in 10 s intervals is shown in Fig. 4.1. The LEEM bright-field images were acquired at the energy of 1.5 eV where both phases have good contrast with respect to the Ag surface and each other. After reaching sufficient temperature, the nucleation of the β-phase starts simultaneously over the sample surface without any preferential nucleation sites. Transformation progresses rapidly compared to the heating rate. Islands

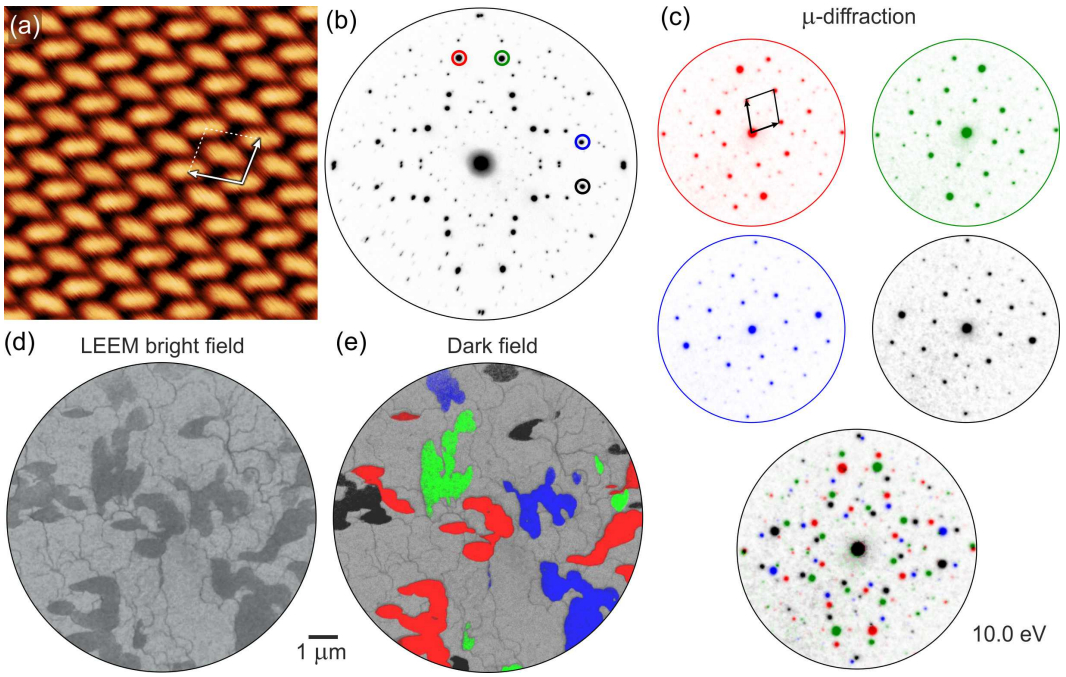


*Fig. 3.11:* (a) STM and (d) LEEM image of the β-phase. (b) Wide area diffraction captured at 10 eV. (c) Diffraction pattern taken from individual molecular islands and their composition with the wide area diffraction below. (e) Composition of 4 dark field images taken from diffraction spots marked in the (b).

of the β-phase grow larger at the expense of the α-phase in their close proximity. They appear to create a capture zone in which the α-phase islands quickly dissolve, however the α-phase islands outside of the zone remain intact. This process is significantly affected by the surface atomic steps which are hindering the diffusion of the molecules in the 2D gas. Therefore, at the more stepped surface, as shown in Fig. 4.1(b), the β-phase grows in smaller islands. Here, the nucleation is forced on atomic terraces after reaching sufficient saturation of transformed molecules. Typical phase transition can be viewed in supplementary video file no. 4 (*4-AlphaToBeta.avi*)

Description of the other phases and phase transitions can be found in the full version of the thesis.

# 4. MOLECULAR NETWORKS ON GRAPHENE

The goal of the experimental work presented in this chapter is the preparation of Ni-TCNQ metal-organic layer on graphene. On metal surfaces, the Ni-TCNQ (7,7,8,8-tetra-cyano-quino-dimethane) molecular network exhibit weak ferromagnetic coupling [62]. The coupling was explained in terms of indirect coupling mediated by the conduction electrons, i.e., Ruderman-Kittel-Kasuya-Yosida (RKKY) interactions [63], or in terms of superexchange via the negatively charged ligand [64]. The tunability of the Fermi level position in graphene and consequently the electronic states in Ni-TCNQ system in its vicinity could theoretically enable external control of the magnetic coupling for application in spintronics and quantum processing [65, 66].

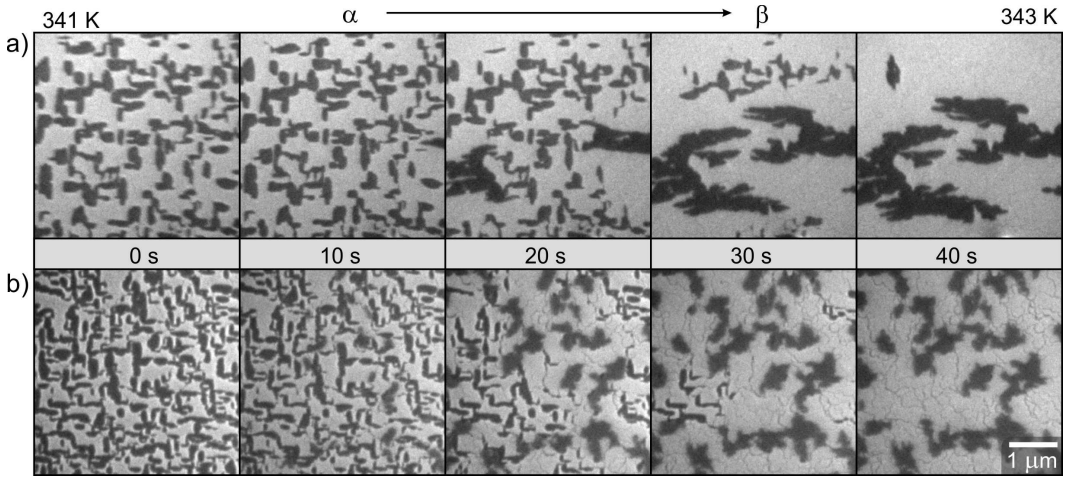


*Fig. 4.1:* Bright field LEEM images of $\alpha \Rightarrow \beta$ phase transformation progress in 10 s intervals. Surface of Ag (1 0 0) with small (a) and high (b) atomic step density (different experiments). Images acquired at 1.5 eV.

## *4.1 Graphene synthesis*

The first method used for the graphene fabrication was a micro-mechanical cleavage (often called scotch tape method or exfoliation) of HOPG (highly oriented pyrolytic graphite) utilized by A. Geim and K. Novoselov in 2004 [67], when the graphene was discovered. This method yields single- or multi-layer graphene flakes of micrometre size. It is a time–consuming process which needs additional techniques such as atomic force microscope (AFM) or Raman spectroscopy to verify the thickness and quality of the graphene flakes. The advantage of the exfoliation is a simple production of high-quality graphene [68]. In the following years, many other methods were developed

e.g.: thermal decomposition of SiC [69], liquid-phase exfoliation [70] and molecular beam epitaxy [71]. However, one of the most promising methods for future industrial production of graphene layer are based on the graphene growth on metal substrate.

Graphene growth on metals can be divided into two approaches. One is based on segregation of carbon atoms from the bulk of the metals such as Ru (0 0 0 1)[72] or Pt (1 1 1)[73], during thermal annealing in vacuum. The main problem of the segregation approach lies in achieving exactly one layer due to additional segregated carbon, which often results in thicker, few-layer graphene stacks.

The second approach is based on the thermal decomposition of hydrocarbons catalysed via its adsorption on the surface. Many transition metals are catalytically active and can decompose hydrocarbons at elevated temperatures. Several types of precursors can be used to synthesize graphene such as ethylene [74], PMMA layer [75] or even liquid precursors, e.g. hexane [76].

### *4.1.1 Ultra-high vacuum syntheses*

Studies of graphene growth and properties on the well-defined metallic surfaces in ultra-high vacuum are beneficial for understanding the nucleation, growth processes and interactions of graphene with metals. Use of a clean single crystal as opposed to the polycrystalline foils reduces the number of defects and grain boundaries which interfere with the growth process and damage the graphene crystal structure. In this work, graphene was prepared by combination of temperature-programmed growth (TPG) and CVD. During the TPG growth, hydrocarbon molecules are adsorbed at a room temperature followed by pyrolysis and graphene growth at a fixed elevated temperature. For the purposes of this work, graphene layer was grown in the LEEM chamber, which allowed direct observation of the growth process. Once the growth parameters were optimized, the subsequent depositions were checked only after the growth. In the next step, ethylene is adsorbed on the surface. In order to ensure the full coverage, ethylene pressure was raised to $3-5\times10^{-6}$ mbar for 3 – 5 min.

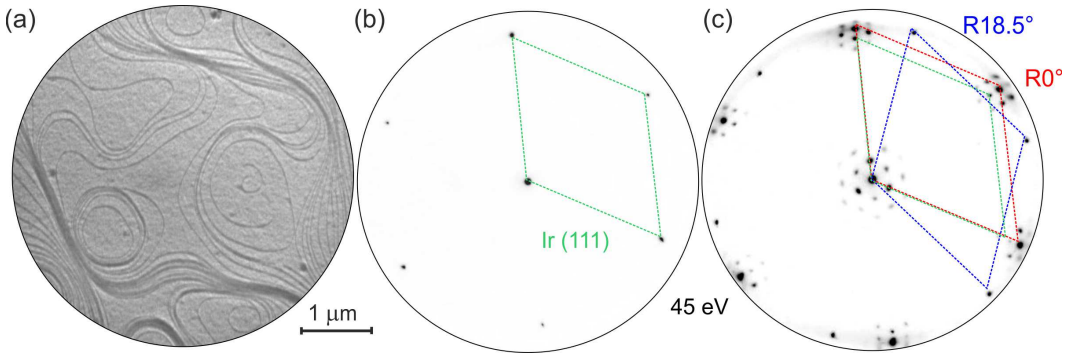


*Fig. 4.2:* (a) Clean Ir (1 1 1) surface with large atomic terraces observed in LEEM at 4 eV. (b) Diffraction pattern coresponding to (a) acquired at 45 eV, Ir reciprocal unit cell marked in green. (c) Diffraction image after the growth of graphene shows typical moire structure of R0° domain marked red and the R18.5° domain marked in blue.

Graphene grows on Ir (1 1 1) preferentially in a way, that densely packed graphene rows are aligned with the densely packed substrate rows (referred to as R0° domain). However, several other graphene islands with a variety of rotational angles in respect to the Ir are also formed [77]. Initial TPG step during the growth leads to the formation of a high density of small aligned R 0 °graphene islands. During the second step of the growth, the CVD, any new graphene domains that impinge on existing nuclei are effectively forced to grow in R0° [78] (observed for $T_{CVD} \sim 1150\,°C$).

After the adsorption of ethylene, the chamber pressure is reduced to $(3-4) \times 10^{-8}$ mbar, which should correspond to approx. $1 \times 10^{-7}$ mbar of ethylene pressure (after correcting for the gauge sensitivity). The second step, the CVD growth then continues by annealing of Ir (1 1 1) crystal to 1150 °C for approx. 12 min.

Combined TPG+CVD growth yields predominantly R0° graphene. However, the resulting quality varies from experiment to experiment. Typically, a broad distribution of rotational domains would show up as Debye-Scherrer rings surrounding the (00)-spot. In our case, the spots often appear broader suggesting variations in graphene orientations around the R0°. Recently, this broader spots were explained as strain minimisation between the graphene layer and the Ir(111) substrate [79]. Graphene lattice parameter remains almost constant at various temperatures [80], meanwhile, the Ir lattice parameter changes. This difference puts compressive stress on the graphene layer, and the resulting strain is relieved by rotations of the graphene lattice.

## 4.2 TCNQ self-assembly on graphene

An initial step towards the preparation of metal-organic Ni-TCNQ network was the study of TCNQ self-assembly on graphene. TCNQ molecule, schematically shown in Fig. 4.3(a), was one of the first molecules to be studied on the graphene in 2010 [10, 81]. The motivation for original TCNQ experiments on graphene was a strong electron acceptor property of TCNQ, leading to a p-doping of graphene. According to theoretical calculations, four cyano groups of TCNQ interact with graphene accepting electrons and in-plane molecular ordering is mediated by attractive electrostatic interactions between the negatively charged cyano groups and the positively charged hydrogen atoms of the central ring [82]. Each molecule form four bonds resulting in a closed packed self-assembled layer on the graphene/Ir (1 1 1) surface. Similar behaviour has been observed for TCNQ self-assembled on Au(1 1 1) [83].

Several samples were prepared with various TCNQ coverages 0.5–1 ML. No molecular islands were observed in real-space images in LEEM, as shown in the Fig. 4.4(a). This is contrary to the experiments on metal surfaces, e.g. on Ag (1 1 1) [84]. However, it was possible to obtain diffraction images shown in Fig. 4.4(b). Observed patterns quickly disappeared after several seconds of measurement, and sample position had to be moved for each new image. Due to the strong electron affinity of TCNQ, it is possible, that electron beam will charge the TCNQ molecules. The increased negative charge accumulated on the cyano groups will then cause repulsion between the

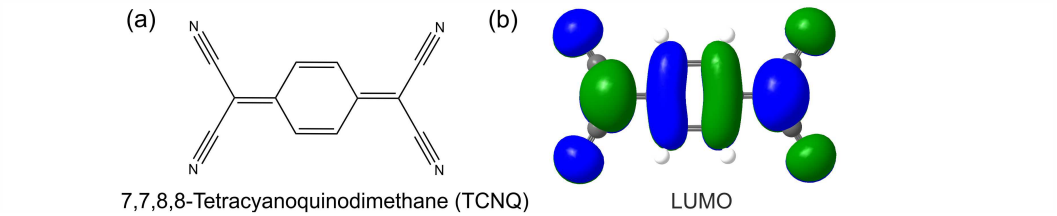


*Fig. 4.3:* (a) Schematic of 7,7,8,8–tetracyanoquinodimethane (TCNQ) molecule. (b) Visualization of the lowest unoccupied molecular orbital (LUMO) of TCNQ molecule in gas phase.

molecules followed by the dissolution of the ordered phase resulting in the eventual disappearance of diffraction spots.

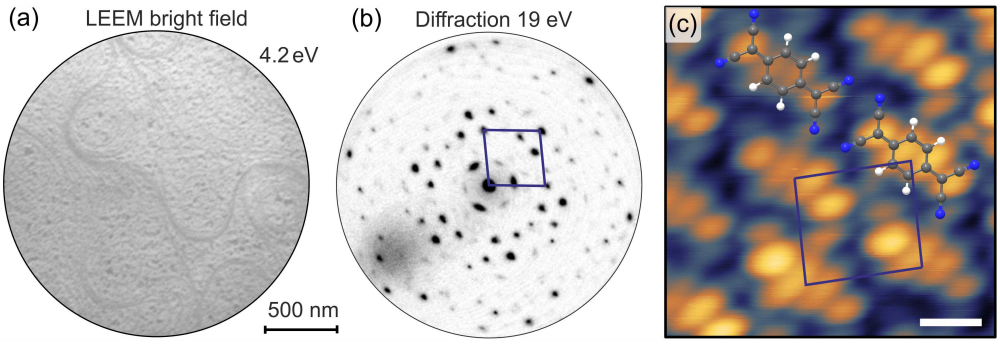


*Fig. 4.4:* (a) LEEM image of approx. 1 ML of TCNQ on graphene/Ir (1 1 1) substrate. No molecular islands are observed. (b) Large area diffraction taken at 19 eV, TCNQ unit cell is marked by blue rhombus. Diffraction pattern can be reproduced by 3 rotationally equivalent phases of TCNQ (each rotated 60°) and additional 3 mirrored ones. (c) STM image of TCNQ on graphene. TCNQ appearance is similar to LUMO state of TCNQ. Scale bar is 0.5 nm.

Self-assembled TCNQ on graphene was reliably imaged in STM Fig. 4.5. The tightly packed structure was identified in agreement with previous experiments on graphene [10]. Similarly to the BDA on graphene, TCNQ self-assembly can cross over the step-edges as shown in Fig. 4.5(a). Here, the image contrast was enhanced by local contrast equalisation to observe all three atomic planes simultaneously. The appearance of TCNQ molecule on graphene was observed to change with applied bias voltage. It appears, that due to the weak molecule-graphene interaction and decoupling from the Ir substrate it is possible to distinguish molecular orbitals at room temperature STM measurements. The most stable measurement conditions, were TCNQ structure appearance was similar to its LUMO (shown in Fig. 4.3(b)), were obtained with scanning parameters: -100 to +200 mV of bias voltage with $I_t \sim 200$ pA. Distance between the molecules in row was measured $12.1 \pm 0.6$ Å and inter-row distance $6.5 \pm 0.3$ Å. Additionally, multiple brighter spots were observed in the STM images at both lower and higher bias voltages. This can be ascribed to electronic modulations in TCNQ induced by underlying graphene moiré structure.

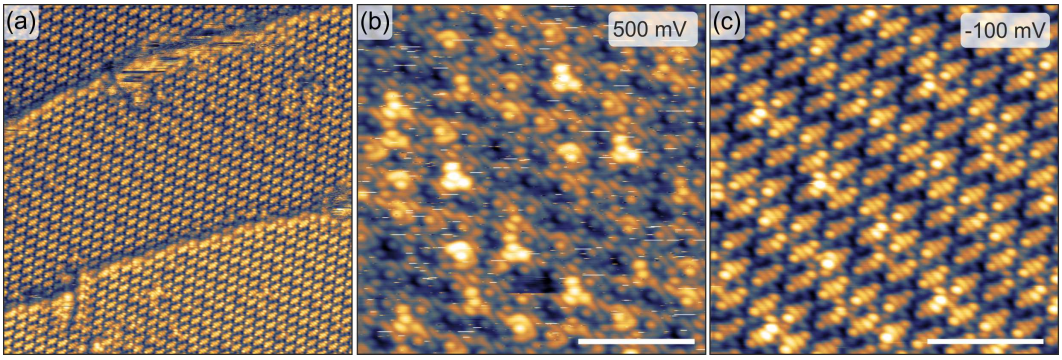


*Fig. 4.5:* STM images of TCNQ self-assembled on graphene/Ir (1 1 1): (a) $30 \times 30\,\mathrm{nm}^2$ image of extended self-assembly order over multiple step edges. (local contrast function was used to visualized all 3 atomic terraces simultaneously); (b) and (c) images of the same area measured at different voltages. Scale bars are 3 nm.

## 4.3 Ni-TCNQ network on graphene

Various metal-TCNQ structures were previously prepared in solution chemistry. The magnetic ordering was observed for synthesized X-TCNQ (X= Mn, Fe, Co, Ni) molecule-based magnets [85]. Additionally, several surface-confined metal-organic structures were prepared, e.g.: Sn-TCNQ on Au (1 1 1) [86], K-TCNQ on Ag (1 1 1), [87] and also Ni-TCNQ on Au (1 1 1) and Ag (1 0 0) [62]. Research of X-TCNQ 2D systems is driven by a broad range of applications such as doping of TCNQ layer[87], possible use as a single-atom catalyst for oxygen reduction [88] or the aforementioned magnetic properties.

Previous experiments had shown, that metal centre incorporated in metal-organic systems recover their magnetic moments [89]. In the Ni-TCNQ network on Au (1 1 1) the ferromagnetic coupling was observed. Theoretical calculation identified the appearance of ferromagnetism in Ni-TCNQ as Heisenberg exchange coupling between spins localised at Ni sites and the itinerant spin density [64]. The itinerant electrons[1] appear due to the spin polarisation of the LUMO band, hybridised with Ni 3d states. An alternative explanation of Ni-TCNQ ferromagnetic behaviour was given in terms of indirect coupling mediated by the conduction electrons, i.e., Ruderman-Kittel-Kasuya-Yosida (RKKY) interaction [63].

Compared to the metal substrate, the use of graphene has the potential to further improve the recovery of magnetic moments in metallic centres. Additional motivation to grow Ni-TCNQ metal-organic system on graphene was the possibility to tune magnetic interaction strength. Theoretical work suggested that the indirect interaction strength can be effectively controlled by adjusting the Fermi level position in graphene with an external gate voltage [65]. Similarly, electronic density on molecular states was shown to be controllable by gate voltage [66] applied on the graphene substrate.

[1] "Ferromagnets, such as those made of iron or nickel, are called itinerant because the electrons whose spins aligned to create the magnetic state are extended and are the same as the ones responsible for conduction." [90]

This could allow control over the superexchange interaction strength as the spin-orbit coupling can be controlled by the subtle change of molecular structure [91].

### 4.3.1 Preparation of Ni-TCNQ network

In order to prepare the Ni-TCNQ coordination network on graphene, TCNQ molecules were deposited, followed by deposition of the Ni atoms with subsequent annealing (20–30 min). The annealing temperature was estimated from the previous experiments to be approx. 130 °C. Exact temperature calibration in XPS later determined that initial reaction takes place already at 110 °C and the structure is chemically stable up to 140 °C. In contrast, the evaporation temperature of pure TCNQ from graphene was tested and was found to be approx. 70 °C. Observation in LEEM did not reveal any surface changes or diffraction spots, apart decreased intensity of the graphene moiré spots. Absence of both real-space and diffraction pattern initially implied that the structure is forming in disordered clusters instead of the ordered 2D layer (similarly to Fe-BDA). However, the STM measurement revealed the presence of small 2D islands ($5 \times 5\,\mathrm{nm}^2$), scattered across graphene.

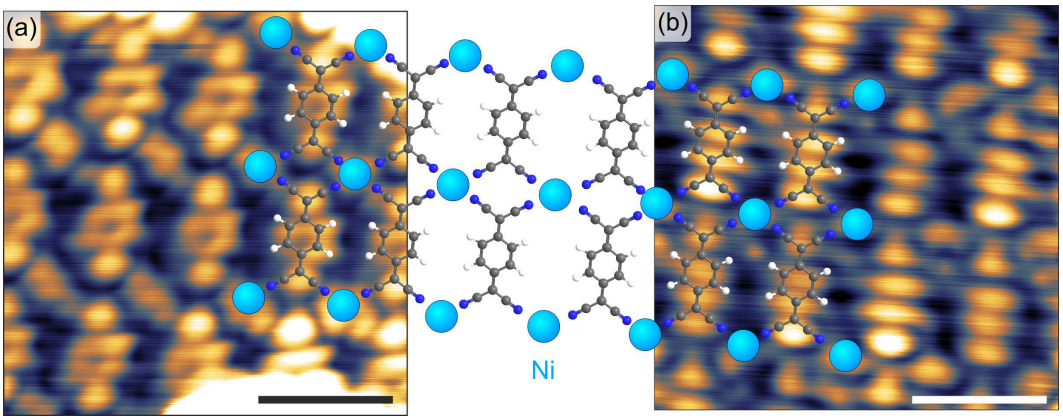


*Fig. 4.6:* STM images of Ni-TCNQ network on graphene/Ir (1 1 1) at different positions. In the image (a) the TCNQ resembles its chemical structure and in the image (b) the LUMO-like state. Scans were taken at similar conditions $U_B = -110\,\mathrm{mV}, I_t = -600\,\mathrm{pA}$ for (a) and $U_B = -90\,\mathrm{mV}, I_t = -450\,\mathrm{pA}$ for (b). Contrast change was attributed to random tip functionalization. Illustration of Ni-TCNQ network is overlaid over the images. Scale bars are 1 nm. Ni atoms are not in scale.

STM topography of Ni-TCNQ network is shown in Fig. 4.6. TCNQ molecules are assembled next to each other, and the additional bright feature can be observed in between. This bright spot was attributed to the Ni atom. Similar coordination network, where four N from cyano groups of TCNQ molecule are binding to Ni atom, was observed on Au (1 1 1) [62]. Presented images show two appearances of TCNQ molecules acquired at similar scanning parameters. In Fig. 4.6(a), the TCNQ resembles its chemical structure. This appearance was attributed the enhanced resolution of STM due to random functionalisation of STM tip. In the image in Fig. 4.6(b) TCNQ resembles it's LUMO-like state, similarly to previously observed structure in pure TCNQ

self-assembled layer on graphene. Distance between the molecules in a row decreased to 10.0 – 10.4 Å, from approx. 12 Å in pure TCNQ phase on graphene, suggesting a significant change in the bonding environment. From the proposed geometry, the N-Ni bond length was roughly estimated to be 1.5 Å, corresponding to previously measured N-Co coordination bond length on graphene 1.5 ± 0.2 Å [92].

In summary, the Ni-TCNQ was reliably prepared with reaction performed with an excess amount of TCNQ to Ni ratio. However, the layer quality, e.i. long-range order was limited, and the resulting structure often appeared as a multi-layer. This was unexpected as at the reaction temperature (> 110 °C) excess TCNQ molecules should desorb from the surface. In the 3D chemistry, the Ni-TCNQ coordination polymers were formed with each Ni ion binding to six different TCNQ molecules. Resulting bonding geometry was significantly different from one observed on surfaces and resulted in a 2D honeycomb-like motif that is further interconnecting to 3D networks [93]. This suggests that there may be a potential for Ni-TCNQ network to extend into the second layer.

### *4.3.2 XPS analysis of Ni-TCNQ network*

XPS analysis was performed to verify the formation of Ni-TCNQ bonds. TCNQ chemical state was analysed through the N 1s peak of the cyano groups. Sample with a larger amount of TCNQ molecules (approx. 2 ML) was prepared in order to achieve sufficient signal to noise ratio. Ni was co-deposited with TCNQ on the hot substrate with the aim to deposit more Ni than required for potential Ni+TCNQ network (approx. 0.1 ML). Changes were observed in the XPS spectra of both N 1s and Ni 3p. The energy the N 1s peak position is shifted toward the lower binding energies by 0.5–0.6 eV. Change towards the lower binding energies by approx. 1 eV was observed in previous studies of TCNQ-metal complexes [94], TCNQ on metallic surfaces [95] or recently Sn-TCNQ coordination structures on metal surfaces [86].

The appearance of the Ni spectra was consistent with a higher oxidation state of Ni, i.e. broad maxima, extended satellite structure and loss of asymmetry. The XPS spectra of higher oxidation states of Ni are not easily identified due to the complex mainline splitting. The simplest $Ni^{2+}$ spectra are typically fitted by complex multiplet envelope (seven components in case of $Ni^{2+}$ Gupta-Sen multiplet) [96, 97]. More precise analysis in our case was not possible due to the weak signal and possible multiple oxidation states in a thicker layer of Ni-TCNQ. Nevertheless, observations of shifts in both N 1s and Ni 3p peak towards lower and higher binding energies, respectively, is a strong indication for the formation of the metal-organic bonds on the graphene/Ir (1 1 1).

# 5. CONCLUSIONS

This thesis presented the first experimental results obtained from a newly installed ultra-high vacuum system dedicated to study of molecular systems on surfaces. Results from multiple self-assembled molecular structures are presented i.e.: (i) BDA on Cu (1 0 0); (ii) BDA on Ag (1 0 0); (i) BDA on graphene/Ir (1 1 1); (iv) TCNQ on graphene/Ir (1 1 1). The first experimental chapter (Chapter 3) is dedicated to the BDA on metallic substrates systems (i-ii), which represents a model system of molecular self-assembly on surfaces. Anomalous growth of BDA on Cu (1 0 0) was observed, where molecular island grew without typical preferential nucleation sites at step edges. It was discovered that step edges of atomic planes are decorated by BDA molecules, and due to specific bonding geometry, this prevents the attachment of self-assembled islands. Therefore, the step edges are effectively passivated and present a diffusion barrier for molecular growth. Additionally presented molecular model was able to explained observed defects in the BDA self-assembled structure.

The BDA on Ag (1 0 0) presented a significantly more complex system, compared to the BDA on Cu (1 0 0), and includes multiple unique phases and phase transitions. The transformations of BDA are driven by thermally induced deprotonation, creating chemically different molecules and changing bonding environment of their self-assembly. Each molecular phase was comprehensively analyzed by STM, AFM, LEEM and XPS, resulting in atomic models for each phase. Additionally, several main phase transformations were described based on real-time observations in LEEM. The phase transformation shows a wide range of phenomena including Ostwald ripening of the α-phase before the transformation, remote dissolution of the α-phase islands in the vicinity of β-phase islands, burst nucleation of $\gamma_3$ phase and internal directional transformation of $\gamma_3$ to $\gamma_2$-phase. Observations of these phenomena could be later employed for modelling of the nucleation and growth in molecular systems featuring weak interactions and specifically applied for molecules functionalized by carboxylic groups.

The BDA self-assembled phases on Ag named here as the δ- , $\gamma_2$- and $\gamma_3$- phases, also represent k-uniform tessellations with 1, 2, and 3 distinct vertex types. A unique feature in the BDA structure compared to other molecular systems is partially deprotonated BDA molecule that mediates connection of two distinct binding motifs in a single self-assembled molecular phase. This determination can help to provide selection rules for designing new molecular networks with novel physical or chemical properties.

Next chapter (Chapter 4) describes the recipe for the growth of high quality single crystalline mono-layer graphene on Ir (1 1 1). Self-assembly of BDA was tested on the graphene on Ir and resulting self-assembled structure was similar to the BDA α-phase

on Ag. However, the molecular islands were growing in multiple directions, seamlessly changing orientation and traversing the step edges due to the inert nature of graphene. Additionally, graphene effectively screens the metallic substrate preserving some of the molecular electronic structure as was observed in STM for TCNQ molecules on graphene. From the diffraction pattern, it was possible to identify multiple rotationally equivalent structures of BDA and TCNQ self-assembly on graphene.

Next sections described attempts to prepare Fe-BDA in most part as a test in preparation for the growth of Ni-TCNQ 2D metal-organic coordination networks. In both cases, the XPS data confirmed a chemical reaction between the molecular species and metal atoms; however, the 2D structure was only observed for TCNQ. The Ni-TCNQ coordination network was formed by four nitrogen atoms from TCNQ cyano groups binding to one Ni atom in a fashion similar to networks prepared on metallic substrates. However, on graphene, only small islands were observed due to weak substrate-molecule interaction that most likely hinders the formation of an extended network. In view of this fact, more robust molecules will be tested in the future. Additionally, the presence of the ferromagnetic coupling between the Ni atoms will be tested by transferring the sample into the state of the art EPR spectroscope. The possibility to tune the Fermi level position of graphene and consequently the electronic states in Ni-TCNQ system in its vicinity could enable externally control the magnetic coupling in the metal-organic systems.

In conclusion, this thesis presented several molecular systems on various surfaces. Most important were observations of structure and phase transformations of BDA on Cu and Ag that may lead to improved applications and theoretical growth models for molecular layers. Another significant result is the growth of 2D Ni-TCNQ metal coordinated network on graphene. Lessons learned here will provide a roadmap for future experimental realizations of structures on non-interacting substrates.

# 6. AUTHORS PUBLICATIONS

*Thesis related articles:*

1) PROCHAZKA, P.; GOSALVEZ, M. A.; **KORMOS, L.**; DE LA TORRE, B.; GALLARDO, A.; ALBERDI-RODRIGUEZ, J.; CHUTORA, T.; MAKOVEEV, A.O.; SHAHSAVAR, A.; ARNAU, A.; JELINEK, P.; CECHAL, J.: Mul tiscale Analysis of Phase Transformations in Self-Assembled Layers of 4,4-Biphenyl Dicarboxylic on the Ag(001) Surface. *ACS Nano*, 2020, 14 (6), p. 7269-7279, ISSN: 1936-0851. https://doi.org/10.1021/acsnano.0c02491.

2) **KORMOS, L.**; PROCHAZKA, P.; MAKOVEEV, A.O. ; CECHAL, J.: Complex k-uniform tilings by a simple bitopic precursor self-assembled on Ag(001). *Nature Comm.*, 2020, 11, p. 1856, ISSN: 2041-1723. https://doi.org/10.1038/s41467-020-15727-6.

3) **KORMOS, L.**; PROCHAZKA, P.; SIKOLA, T.; CECHAL, J.: Molecular Passivation of Substrate Step Edges as Origin of Unusual Growth Behavior of 4,4-Biphenyl Dicarboxylic Acid on Cu(001). *Journal of Physical Chemistry C*, 2018, 122, p. 2815-2820, ISSN: 1932-7447. https://doi.org/10.1021/acs.jpcc.7b11436.

4) EL-SAYED, A.; PIQUERO-ZULAICA, I.; ABD EL-FATTAH, Z. M.; **KORMOS, L.**; ALI, K.; WEBER, A.; BREDE, J.; DE OTEYZA, D. G.; LOBO-CHECA, J.; ORTEGA, E. AND MARTINA, C.: Synthesis of Graphene Nanoribbons on a Kinked Au Surface: Revealing the Frontier Valence Band at the Brillouin Zone Center. *Journal of Physical Chemistry C*, 2020, 124, p. 15474-15480, ISSN: 1932-7447. https://doi.org/10.1021/acs.jpcc.0c02801.

*Other publications:*

5) FIKACEK, J.; PROCHAZKA, P.; STETSOVYCH, V.; PRUSA, S.; VONDRACEK, M.; **KORMOS, L.**; SKALA, T.; VLAIC, P.; CAHA, O.; CARVA, K.; CECHAL, J.; SPRINGHOLZ, G.; HONOLKA, J.: Step-edge assisted large scale FeSe monolayer growth on epitaxial Bi2Se3 thin films. *New Journal of Physics*, 2020, 22, ISSN: 1367-2630. https://iopscience.iop.org/article/10.1088/1367-2630/ab9b59.

6) REDONDO, J.; LAZAR, P.; PROCHAZKA, P.; PRUSA, S.; MALLADA, B.; CAHLIK, A.; LACHNITT, J.; BERGER, J.; SMID, B.; **KORMOS, L.**; JELINEK, A.; CECHAL, J.; SVEC, M.: Identification of Two-Dimensional $FeO_2$ Termination of Bulk Hematite $\alpha$ – $Fe_2O_3$ (0001) Surface. Journal of Physical Chemistry C, 2019, 123 (23), 14312-14318, ISSN: 1932-7447. https://doi.org/10.1021/acs.jpcc.9b00244.

7) **KORMOS, L.**; KRATZER, M.; KOSTECKI, K.; OEME, M.; SIKOLA, T.; KASPER, E.; SCHULZE, J.; TEICHERT, C.: Surface analysis of epitaxially grown GeSn alloys with Sn contents between 15% and 18%. *Surface and Interface Analysis*, 2017, 49 (4), 297-302, ISSN: 1096-9918. http://dx.doi.org/10.1002/sia.6134.

8) BARTOSIK, M.; **KORMOS, L.**; FLAJSMAN, L.; KALOUSEK, R.; MACH, J.; LISKOVA, Z.; NEZVAL, D.; SVARC, V.; SAMORIL, T.; SIKOLA, T.: Nanometer-Sized Water Bridge and Pull-Off Force in AFM at Different Relative Humidities: Reproducibility Measurement and Model Based on Surface Tension Change. *Journal of Physical Chemistry B*, 2017, 121 (3), 610-619, ISSN: 1520-6106. http://dx.doi.org/10.1021/acs.jpcb.6b11108.

9) MACH, J.; PROCHAZKA, P.; BARTOSIK, M.; NEZVAL, D.; PIASTEK, J.; HULVA, J.; SVARC, V.; KONECNY, M.: **KORMOS, L.**; SIKOLA, T. Electronic transport properties of graphene doped by gallium. *Nanotechnology*, 2017, 28 (41), 1-10, ISSN: 0957-4484. http://dx.doi.org/10.1088/1361-6528/aa86a4.

# BIBLIOGRAPHY


[1] Moore, G. E. Cramming more components onto integrated circuits, reprinted from electronics, volume 38, number 8, april 19, 1965, pp.114 ff. *IEEE Solid-State Circuits Society Newsletter 11*, 3 (2006), 33–35.

[2] Mitchell, W. The chips are down for moore's law. *NATURE NEWS 530* (Feb 2016). https://www.nature.com/news/the-chips-are-down-for-moore-s-law-1.19338.

[3] Topaloglu R. O., Wong, P. *Beyond–CMOS Technologies for Next Generation Computer Design*. Springer, 2019. ISBN 978-3-319-90384-2. doi: doi.org/10.1007/978-3-319-90385-9.

[4] Collier, C. P., Wong, E. W., Belohradský, M., Raymo, F. M., Stoddart, J. F., Kuekes, P. J., Williams, R. S., and Heath, J. R. Electronically configurable molecular-based logic gates. *Science 285*, 5426 (Jul 1999), 391. doi: 10.1126/science.285.5426.391.

[5] METZGER, R. M., and CAVA, M. P. Rectification by a single molecule of hexadecylquinolinium tricyanoquinodimethanide. *Annals of the New York Academy of Sciences 852*, 1 (Jun 1998), 95–115. doi: 10.1111/j.1749-6632.1998.tb09866.x.

[6] Chen, J., Reed, M. A., Rawlett, A. M., and Tour, J. M. Large on-off ratios and negative differential resistance in a molecular electronic device. *Science 286*, 5444 (Nov 1999), 1550. doi: 10.1126/science.286.5444.1550.

[7] Bader, K., Dengler, D., Lenz, S., Endeward, B., Jiang, S.-D., Neugebauer, P., and van Slageren, J. Room temperature quantum coherence in a potential molecular qubit. *Nature Communications 5*, 1 (Oct 2014), 5304. doi: 10.1038/ncomms6304.

[8] Ferrando-Soria, J., Moreno Pineda, E., Chiesa, A., Fernandez, A., Magee, S. A., Carretta, S., Santini, P., Vitorica-Yrezabal, I. J., Tuna, F., Timco, G. A., McInnes, E. J., and Winpenny, R. E. A modular design of molecular qubits to implement universal quantum gates. *Nature Communications 7*, 1 (Apr 2016), 11377. doi: 10.1038/ncomms11377.

[9] Geim, A. K. Graphene: Status and prospects. *Science 324*, 5934 (2009), 1530–1534. doi: 10.1126/science.1158877.

[10] Barja, S., Garnica, M., Hinarejos, J. J., Vázquez de Parga, A. L., Martín, N., and Miranda, R. Self-organization of electron acceptor molecules on graphene. *Chemical Communications 46*, 43 (2010), 8198–8200. doi: 10.1039/C0CC02675A.

[11] Haugen, H., Huertas-Hernando, D., and Brataas, A. Spin transport in proximity-induced ferromagnetic graphene. *Physical Review B 77* (Mar 2008), 115406. doi: 10.1103/PhysRevB.77.115406.

[12] Zhou, B., Chen, X., Wang, H., Ding, K.-H., and Zhou, G. Magnetotransport and current-induced spin transfer torque in a ferromagnetically contacted graphene. *Journal of Physics: Condensed Matter 22*, 44 (Oct 2010), 445302. doi: 10.1088/0953-8984/22/44/445302.

[13] Riss, A., Wickenburg, S., Tan, L. Z., Tsai, H.-Z., Kim, Y., Lu, J., Bradley, A. J., Ugeda, M. M., Meaker, K. L., Watanabe, K., Taniguchi, T., Zettl, A., Fischer, F. R., Louie, S. G., and Crommie, M. F. Imaging and tuning molecular levels at the surface of a gated graphene device. *ACS Nano 8*, 6 (Jun 2014), 5395–5401. doi: 10.1021/nn501459v.

[14] Barth, J. V., Costantini, G., and Kern, K. Engineering atomic and molecular nanostructures at surfaces. *Nature 437*, 7059 (Sep 2005), 671–679. doi: 10.1038/nature04166.

[15] Barth, J. V. Molecular architectonic on metal surfaces. *Annual Review of Physical Chemistry 58*, 1 (May 2007), 375–407. doi: 10.1146/annurev.physchem.56.092503.141259.

[16] Dong, L., Gao, Z., and Lin, N. Self-assembly of metal–organic coordination structures on surfaces. *Progress in Surface Science 91*, 3 (Aug 2016), 101–135. doi: 10.1016/j.progsurf.2016.08.001.

[17] Jelínek, P. High resolution spm imaging of organic molecules with functionalized tips. *Journal of Physics: Condensed Matter 29*, 34 (Jul 2017), 343002. doi: 10.1088/1361-648x/aa76c7.

[18] Van Vleet, M. J., Misquitta, A. J., Stone, A. J., and Schmidt, J. R. Beyond born–mayer: Improved models for short-range repulsion in ab initio force fields. *Journal of Chemical Theory and Computation 12*, 8 (Aug 2016), 3851–3870. doi: 10.1021/acs.jctc.6b00209.

[19] Stone, A. *The Theory of Intermolecular Forces*. OUP Oxford, 2013. 2nd edition, ISBN: 9780199672394.

[20] Israelachvili, J. N. *Intermolecular and Surface Forces*, 3rd revised ed. Academic Press, 2011. ISBN: 0123919274, 9780123919274.

[21] Zambelli, T., Goudeau, S., Lagoute, J., Gourdon, A., Bouju, X., and Gauthier, S. Molecular self-assembly of jointed molecules on a metallic substrate: From single molecule to monolayer. *ChemPhysChem 7*, 9 (Sep 2006), 1917–1920. doi: 10.1002/cphc.200600349.

[22] Gravil, P. A., Devel, M., Lambin, P., Bouju, X., Girard, C., and Lucas, A. A. Adsorption of $c_{60}$ molecules. *Physical Review B 53* (Jan 1996), 1622–1629. doi: 10.1103/PhysRevB.53.1622.

[23] Grimme, S., Antony, J., Ehrlich, S., and Krieg, H. A consistent and accurate ab initio parametrization of density functional dispersion correction (dft-d) for the 94 elements h-pu. *The Journal of Chemical Physics 132*, 15 (Apr 2010), 154104. doi: 10.1063/1.3382344.

[24] Steiner, T. The hydrogen bond in the solid state. *Angewandte Chemie International Edition 41*, 1 (Jan 2002), 48–76. doi: 10.1002/1521-3773(20020104)41:1<48::AID-ANIE48>3.0.CO;2-U.

[25] Mo, Y. Probing the nature of hydrogen bonds in dna base pairs. *Journal of Molecular Modeling 12*, 5 (Jul 2006), 665–672. doi: 10.1007/s00894-005-0021-y.

[26] Taylor, R., and Kennard, O. Crystallographic evidence for the existence of ch.cntdot..cntdot..cntdot.o, ch.cntdot..cntdot..cntdot.n and ch.cntdot..cntdot..cntdot.cl hydrogen bonds. *Journal of the American Chemical Society 104*, 19 (Sep 1982), 5063–5070. doi: 10.1021/ja00383a012.

[27] Arunan, E., Desiraju, G. R., Klein, R. A., Sadlej, J., Scheiner, S., Alkorta, I., Clary, D. C., Crabtree, R. H., Dannenberg, J. J., Hobza, P., Kjaergaard, H. G., Legon, A. C., Mennucci, B., and Nesbitt, D. J. Definition of the hydrogen bond (iupac recommendations 2011). *Pure and Applied Chemistry 83*, 8 (2011), 1637–1641. doi: 10.1351/PAC-REC-10-01-02.

[28] Hunter, C. A., and Sanders, J. K. The nature of π-π interactions. *Journal of the American Chemical Society 112*, 14 (1990), 5525–5534. doi: doi.org/10.1021/ja00170a016.

[29] Tsuzuki, S., Honda, K., Uchimaru, T., Mikami, M., and Tanabe, K. Origin of attraction and directionality of the $\pi/\pi$ interaction: model chemistry calculations of benzene dimer interaction. *Journal of the American Chemical Society 124*, 1 (Jan 2002), 104–112. doi: 10.1021/ja0105212.

[30] Meyer, E. A., Castellano, R. K., and Diederich, F. Interactions with aromatic rings in chemical and biological recognition. *Angewandte Chemie International Edition 42*, 11 (Mar 2003), 1210–1250. doi: 10.1002/anie.200390319.

[31] Schiffrin, A., Riemann, A., Auwärter, W., Pennec, Y., Weber-Bargioni, A., Cvetko, D., Cossaro, A., Morgante, A., and Barth, J. V. Zwitterionic self-assembly of l-methionine nanogratings on the ag(111) surface. *Proceedings of the National Academy of Sciences 104*, 13 (2007), 5279–5284. doi: 10.1073/pnas.0607867104.

[32] Won, S.-Y., Kim, J.-H., Kim, H., Yoon, J. K., Kahng, S.-J., Kwon, Y.-K., and Park, Y. Linear and Hexagonal Porous Structures of an Organic Charge Acceptor Hexaaza-triphenylene-hexacarbonitrile on Au(111) with CNÂ · Â · Â · CN Dipolar Interactions. *The Journal of Physical Chemistry C 117*, 41 (Oct. 2013), 21371–21375. doi: 10.1021/jp407173w.

[33] Ishii, H., Oji, H., Ito, E., Hayashi, N., Yoshimura, D., and Seki, K. Energy level alignment and band bending at model interfaces of organic electroluminescent devices. *Journal of Luminescence 87-89* (May 2000), 61–65. doi: 10.1016/S0022-2313(99)00230-6.

[34] Bartels, L. Tailoring molecular layers at metal surfaces. *Nature Chemistry 2*, 2 (Feb 2010), 87–95. doi: 10.1038/nchem.517.

[35] Li, Y., Xiao, J., Shubina, T. E., Chen, M., Shi, Z., Schmid, M., Steinrück, H.-P., Gottfried, J. M., and Lin, N. Coordination and metalation bifunctionality of cu with 5,10,15,20-tetra(4-pyridyl)porphyrin: Toward a mixed-valence two-dimensional coordination network. *Journal of the American Chemical Society 134*, 14 (Apr 2012), 6401–6408. doi: 10.1021/ja300593w.

[36] Stepanow, S., Strunskus, T., Lingenfelder, M., Dmitriev, A., Spillmann, H., Lin, N., Barth, J. V., Wöll, C., and Kern, K. Deprotonation driven phase transformations in terephthalic acid self assembly on cu(100). *The Journal of Physical Chemistry B 108*, 50 (2004), 19392–19397. doi: 10.1021/jp046766t.

[37] Schmitt, T., Hammer, L., and Schneider, M. A. Evidence for on-site carboxylation in the self-assembly of 4,4-biphenyl dicarboxylic acid on cu(111). *The Journal of Physical Chemistry C 120*, 2 (Jan 2016), 1043–1048. doi: 10.1021/acs.jpcc.5b10394.

[38] Cao, N., Ding, J., Yang, B., Zhang, J., Peng, C., Lin, H., Zhang, H., Li, Q., and Chi, L. Deprotonation-induced phase evolutions in co-assembled molecular structures. *Langmuir 34*, 26 (Jul 2018), 7852–7858. doi: 10.1021/acs.langmuir.8b00228.

[39] Quiroga Argañaraz, B., Cristina, L. J., Rodríguez, L. M., Cossaro, A., Verdini, A., Floreano, L., Fuhr, J. D., Gayone, J. E., and Ascolani, H. Ubiquitous deprotonation of terephthalic acid in the self-assembled phases on cu(100). *Physical Chemistry Chemical Physics 20*, 6 (2018), 4329–4339. doi: 10.1039/C7CP06612K.

[40] Schnadt, J., Xu, W., Vang, R. T., Knudsen, J., Li, Z., Lægsgaard, E., and Besenbacher, F. Interplay of adsorbate-adsorbate and adsorbate-substrate interactions in self-assembled molecular surface nanostructures. *Nano Research 3*, 7 (2010), 459–471. doi: 10.1007/s12274-010-0005-9.

[41] Cechal, J., Kley, C. S., Kumagai, T., Schramm, F., Ruben, M., Stepanow, S., and Kern, K. Convergent and divergent two-dimensional coordination networks formed through substrate-activated or quenched alkynyl ligation. *Chemical Communications 50*, 69 (2014), 9973–9976. doi: 10.1039/C4CC03723E.

[42] Kley, C. S., Cechal, J., Kumagai, T., Schramm, F., Ruben, M., Stepanow, S., and Kern, K. Highly adaptable two-dimensional metal-organic coordination networks on metal surfaces. *Journal of the American Chemical Society 134*, 14 (Apr 2012), 6072–6075. doi: 10.1021/ja211749b.

[43] Zhou, X., Wang, C., Zhang, Y., Cheng, F., He, Y., Shen, Q., Shang, J., Shao, X., Ji, W., Chen, W., Xu, G., and Wu, K. Steering surface reaction dynamics with a self-assembly strategy: Ullmann coupling on metal surfaces. *Angewandte Chemie International Edition 56*, 42 (Oct 2017), 12852–12856. doi: 10.1002/anie.201705018.

[44] Cañas-Ventura, M. E., Klappenberger, F., Clair, S., Pons, S., Kern, K., Brune, H., Strunskus, T., Wöll, C., Fasel, R., and Barth, J. V. Coexistence of one- and two-dimensional supramolecular assemblies of terephthalic acid on pd(111) due to self-limiting deprotonation. *The Journal of Chemical Physics 125*, 18 (Nov 2006), 184710. doi: 10.1063/1.2364478.

[45] Fortuna, S., and Troisi, A. Agent-based modeling for the 2d molecular self-organization of realistic molecules. *The Journal of Physical Chemistry B 114*, 31 (2010), 10151–10159. doi: 10.1021/jp103950m.

[46] Stepanow, S., Lin, N., Vidal, F., Landa, A., Ruben, M., Barth, J. V., and Kern, K. Programming supramolecular assembly and chirality in two-dimensional dicarboxylate networks on a cu(100) surface. *Nano Letters 5*, 5 (May 2005), 901–904. doi: 10.1021/nl050362a.

[47] Lingenfelder, M. A., Spillmann, H., Dmitriev, A., Stepanow, S., Lin, N., Barth, J. V., and Kern, K. Towards surface-supported supramolecular architectures: Tailored coordination assembly of 1,4-benzenedicarboxylate and fe on cu(100). *Chemistry - A European Journal 10*, 8 (Apr 2004), 1913–1919. doi: 10.1002/chem.200305589.

[48] Wagner, S. R., Lunt, R. R., and Zhang, P. Anisotropic crystalline organic step-flow growth on deactivated si surfaces. *Physical Review Letter 110* (Feb 2013), 086107. doi: 10.1103/PhysRevLett.110.086107.

[49] Schwarz, D., van Gastel, R., Zandvliet, H. J. W., and Poelsema, B. Growth anomalies in supramolecular networks: $4,4'$-biphenyldicarboxylic acid on cu(001). *Physical Review Letter 110* (Feb 2013), 076101. doi: 10.1103/PhysRevLett.110.076101.

[50] Faraggi, M. N., Rogero, C., Arnau, A., Trelka, M., Écija, D., Isvoranu, C., Schnadt, J., Marti-Gastaldo, C., Coronado, E., Gallego, J. M., Otero, R., and Miranda, R. Role of deprotonation and cu adatom migration in determining the reaction pathways of oxalic acid adsorption on cu(111). *The Journal of Physical Chemistry C 115*, 43 (Nov 2011), 21177–21182. doi: 10.1021/jp205779g.

[51] Fuhr, J. D., Carrera, A., Murillo-Quirós, N., Cristina, L. J., Cossaro, A., Verdini, A., Floreano, L., Gayone, J. E., and Ascolani, H. Interplay between hydrogen bonding and molecule-substrate interactions in the case of terephthalic acid molecules on cu(001) surfaces. *The Journal of Physical Chemistry C 117*, 3 (Jan 2013), 1287–1296. doi: 10.1021/jp305455v.

[52] Wang, H., Buller, O., Wang, W., Heuer, A., Zhang, D., Fuchs, H., and Chi, L. Area confined position control of molecular aggregates. *New Journal of Physics 18*, 5 (2016), 053006. doi: 10.1088/1367-2630/18/5/053006.

[53] Schlickum, U., Decker, R., Klappenberger, F., Zoppellaro, G., Klyatskaya, S., Ruben, M., Silanes, I., Arnau, A., Kern, K., Brune, H., and Barth, J. V. Metal-organic honeycomb nanomeshes with tunable cavity size. *Nano Letters 7*, 12 (Dec 2007), 3813–3817. doi: 10.1021/nl072466m.

[54] Gaberle, J., Gao, D. Z., Shluger, A. L., Amrous, A., Bocquet, F., Nony, L., Para, F., Loppacher, C., Lamare, S., and Cherioux, F. Morphology and growth mechanisms of self-assembled films on insulating substrates: Role of molecular flexibility and entropy. *The Journal of Physical Chemistry C 121*, 8 (Mar 2017), 4393–4403. doi: 10.1021/acs.jpcc.6b12738.

[55] Khokhar, F. S., van Gastel, R., Schwarz, D., Zandvliet, H. J. W., and Poelsema, B. A low energy electron microscopy study of the initial growth, structure and thermal stability of bda-domains on cu(001). *Journal of chemical physics 135*, 12 (2011). Article. doi: 10.1063/1.3641893.

[56] Tait, S. L., Lim, H., Theertham, A., and Seidel, P. First layer compression and transition to standing second layer of terephthalic acid on cu(100). *Physical Chemistry Chemical Physics 14*, 22 (2012), 8217–8223. doi: 10.1039/C2CP41256J.

[57] Menzel, D. The development of core electron spectroscopies of adsorbates. *Surface Science 299-300* (1994), 170–182. doi: 10.1016/0039-6028(94)90653-X.

[58] Payer, D., Comisso, A., Dmitriev, A., Strunskus, T., Lin, N., Wöll, C., DeVita, A., Barth, J. V., and Kern, K. Ionic hydrogen bonds controlling two-dimensional supramolecular systems at a metal surface. *Chemistry - A European Journal 13*, 14 (May 2007), 3900–3906. doi: 10.1002/chem.200601325.

[59] Franke, M., Marchini, F., Zhang, L., Tariq, Q., Tsud, N., Vorokhta, M., Vondrácek, M., Prince, K., Röckert, M., Williams, F. J., Steinruck, H.-P., and Lytken, O. Temperature-dependent reactions of phthalic acid on ag(100). *The Journal of Physical Chemistry C 119*, 41 (Oct 2015), 23580–23585. doi: 10.1021/acs.jpcc.5b07858.

[60] van der Lit, J., Di Cicco, F., Hapala, P., Jelinek, P., and Swart, I. Submolecular resolution imaging of molecules by atomic force microscopy: The influence of the electrostatic force. *Physical Review Letter 116* (Mar 2016), 096102. doi: 10.1103/PhysRevLett.116.096102.

[61] Hermann, K., and Van Hove, M. Leedpat utility, version 4.2. LEED pattern analyzer software available from: `http://www.fhi-berlin.mpg.de/KHsoftware/LEEDpat/index.html`.

[62] Abdurakhmanova, N., Tseng, T.-C., Langner, A., Kley, C. S., Sessi, V., Stepanow, S., and Kern, K. Superexchange-mediated ferromagnetic coupling in two-dimensional ni-tcnq networks on metal surfaces. *Physical Review Letter 110* (Jan 2013), 027202. doi: 10.1103/PhysRevLett.110.027202.

[63] Giovanelli, L., Savoyant, A., Abel, M., Maccherozzi, F., Ksari, Y., Koudia, M., Hayn, R., Choueikani, F., Otero, E., Ohresser, P., Themlin, J.-M., Dhesi, S. S., and Clair, S. Magnetic coupling and single-ion anisotropy in surface-supported mn-based metal–organic networks. *The Journal of Physical Chemistry C 118*, 22 (Jun 2014), 11738–11744. doi: 10.1021/jp502209q.

[64] Faraggi, M. N., Golovach, V. N., Stepanow, S., Tseng, T.-C., Abdurakhmanova, N., Kley, C. S., Langner, A., Sessi, V., Kern, K., and Arnau, A. Modeling ferro- and antiferromagnetic interactions in metal–organic coordination networks. *The Journal of Physical Chemistry C 119*, 1 (Jan 2015), 547–555. doi: 10.1021/jp512019w.

[65] Krainov, I. V., Rozhansky, I. V., Averkiev, N. S., and Lähderanta, E. Indirect exchange interaction between magnetic adatoms in graphene. *Physical Review B 92* (Oct 2015), 155432. doi: 10.1103/PhysRevB.92.155432.

[66] Wickenburg, S., Lu, J., Lischner, J., Tsai, H.-Z., Omrani, A. A., Riss, A., Karrasch, C., Bradley, A., Jung, H. S., Khajeh, R., Wong, D., Watanabe, K., Taniguchi, T., Zettl, A., Neto, A. C., Louie, S. G., and Crommie, M. F. Tuning charge and correlation effects for a single molecule on a graphene device. *Nature Communications 7*, 1 (Nov 2016), 13553. doi: 10.1038/ncomms13553.

[67] Novoselov, K. S., Geim, a. K., Morozov, S. V., Jiang, D., Zhang, Y., Dubonos, S. V., Grigorieva, I. V., and Firsov, A. Electric field effect in atomically thin carbon films. *Science (New York, N.Y.) 306*, 5696 (2004), 666–669. doi: 10.1126/science.1102896.

[68] Novoselov, K. S., Geim, a. K., Morozov, S. V., Jiang, D., Katsnelson, M. I., Grigorieva, I. V., Dubonos, S. V., and Firsov, A. Two-dimensional gas of massless Dirac fermions in graphene. *Nature 438*, 7065 (2005), 197–200. doi: 10.1038/nature04233.

[69] Berger, C., Song, Z., Li, T., Li, X., Ogbazghi, A. Y., Feng, R., Dai, Z., Marchenkov, A. N., Conrad, E. H., First, P. N., and de Heer, W. A. Ultrathin epitaxial graphite 2d electron gas properties and a route toward graphene based nanoelectronics. *The Journal of Physical Chemistry B 108*, 52 (2004), 19912–19916. doi: 10.1021/jp040650f.

[70] Hernandez, Y., Nicolosi, V., Lotya, M., Blighe, F. M., Sun, Z., De, S., T., M., Holland, B., Byrne, M., Gun'Ko, Y. K., Boland, J. J., Niraj, P., Duesberg, G., Krishnamurthy, S., Goodhue, R., Hutchison, J., Scardaci, V., Ferrari, A. C., and Coleman, J. N. High yield production of graphene by liquid phase exfoliation of graphite. *Nat Nano 3*, 9 (2008), 563–568. doi: 10.1038/nnano.2008.215.

[71] Moreau, E., Godey, S., Ferrer, F. J., Vignaud, D., Wallart, X., Avila, J., Asensio, M. C., Bournel, F., and Gallet, J.-J. Graphene growth by molecular beam epitaxy on the carbon-face of sic. *Applied Physics Letters 97*, 24 (2010), 241907. doi: 10.1063/1.3526720.

[72] Marchini, S., Günther, S., and Wintterlin, J. Scanning tunneling microscopy of graphene on ru(0001). *Physical Review B 76* (2007), 075429. doi: 10.1103/PhysRevB.76.075429.

[73] Sutter, P., Sadowski, J. T., and Sutter, E. Graphene on pt(111): Growth and substrate interaction. *Physical Review B 80* (2009), 245411. doi: 10.1103/PhysRevB.80.245411.

[74] N-Diaye, A., Coraux, J., Plasa, T. N., Busse, C., and Michely, T. Structure of epitaxial graphene on ir(111). *New Journal of Physics 10*, 4 (2008), 043033. doi: 10.1088/1367-2630/10/4/043033.

[75] Sun, Z., Yan, Z., Yao, J., Beitler, E., Zhu, Y., and Tour, J. M. Growth of graphene from solid carbon sources. *Nature 468*, 7323 (2010), 549–552. doi: 10.1038/nature09579.

[76] Srivastava, A., Galande, C., Ci, L., Song, L., Rai, C., Jariwala, D., Kelly, K. F., and Ajayan, P. M. Novel liquid precursor-based facile synthesis of large-area continuous, single, and few-layer graphene films. *Chemistry of Materials 22*, 11 (2010), 3457–3461. doi: 10.1021/cm101027c.

[77] Loginova, E., Nie, S., Thürmer, K., Bartelt, N. C., and McCarty, K. F. Defects of graphene on ir(111): Rotational domains and ridges. *Physical Review B 80* (2009), 085430. doi: 10.1103/PhysRevB.80.085430.

[78] van Gastel, R., N'Diaye, A. T., Wall, D., Coraux, J., Busse, C., Buckanie, N. M., Meyer zu Heringdorf, F.-J., Horn von Hoegen, M., Michely, T., and Poelsema, B. Selecting a single orientation for millimeter sized graphene sheets. *Applied Physics Letters 95*, 12 (Sep 2009), 121901. doi: 10.1063/1.3225554.

[79] Omambac, K. M., Hattab, H., Brand, C., Jnawali, G., N'Diaye, A. T., Coraux, J., van Gastel, R., Poelsema, B., Michely, T., Meyer zu Heringdorf, F.-J., and Hoegen, M. H.-v. Temperature-controlled rotational epitaxy of graphene. *Nano Letters 19*, 7 (Jul 2019), 4594–4600. doi: 10.1021/acs.nanolett.9b01565.

[80] Süle, P., Szendrő, M., Hwang, C., and Tapasztó, L. Rotation misorientated graphene moiré superlattices on cu (111): Classical molecular dynamics simulations and scanning tunneling microscopy studies. *Carbon 77* (Oct 2014), 1082–1089. doi: 10.1016/j.carbon.2014.06.024.

[81] Sun, J. T., Lu, Y. H., Chen, W., Feng, Y. P., and Wee, A. T. S. Linear tuning of charge carriers in graphene by organic molecules and charge-transfer complexes. *Physical Review B 81* (Apr 2010), 155403. doi: 10.1103/PhysRevB.81.155403.

[82] de Oliveira, I. S. S., and Miwa, R. H. Organic molecules deposited on graphene: A computational investigation of self-assembly and electronic structure. *The Journal of Chemical Physics 142*, 4 (Jan 2015), 044301. doi: 10.1063/1.4906435.

[83] Umbach, T. R., Fernandez-Torrente, I., Ladenthin, J. N., Pascual, J. I., and Franke, K. J. Enhanced charge transfer in a monolayer of the organic charge transfer complex ttf–tnap on au(111). *Journal of Physics: Condensed Matter 24*, 35 (Aug 2012), 354003. doi: 10.1088/0953-8984/24/35/354003.

[84] Blowey, P. J., Haags, A., Rochford, L. A., Felter, J., Warr, D. A., Duncan, D. A., Lee, T.-L., Costantini, G., Kumpf, C., and Woodruff, D. P. Characterization of growth and structure of tcnq phases on ag(111). *Phys. Rev. Materials 3* (Nov 2019), 116001. doi: 10.1103/PhysRevMaterials.3.116001.

[85] Vickers, E. B., Giles, I. D., and Miller, J. S. M[tcnq]y-based magnets (m = mn, fe, co, ni; tcnq = 7,7,8,8-tetracyano-p-quinodimethane). *Chemistry of Materials 17*, 7 (Apr 2005), 1667–1672. doi: 10.1021/cm047869r.

[86] Rodríguez, L. M., Fuhr, J. D., Machaín, P., Ascolani, H., Lingenfelder, M., and Gayone, J. E. Building two-dimensional metal–organic networks with tin. *Chemical Communications 55*, 3 (2019), 345–348. doi: 10.1039/C8CC08280D.

[87] Haags, A., Rochford, L. A., Felter, J., Blowey, P. J., Duncan, D. A., Woodruff, D. P., and Kumpf, C. Growth and evolution of tetracyanoquinodimethane and potassium coadsorption phases on ag(111). *New Journal of Physics 22*, 6 (Jun 2020), 063028. doi: 10.1088/1367-2630/ab825f.

[88] Deng, Q., Zhao, J., Wu, T., Chen, G., Hansen, H. A., and Vegge, T. 2d transition metal–tcnq sheets as bifunctional single-atom catalysts for oxygen reduction and evolution reaction. *Journal of Catalysis 370* (Feb 2019), 378–384. doi: 10.1016/j.jcat.2018.12.012.

[89] Gambardella, P., Stepanow, S., Dmitriev, A., Honolka, J., de Groot, F. M. F., Lingenfelder, M., Gupta, S. S., Sarma, D. D., Bencok, P., Stanescu, S., Clair, S., Pons, S., Lin, N., Seitsonen, A. P., Brune, H., Barth, J. V., and Kern, K. Supramolecular control of the magnetic anisotropy in two-dimensional high-spin fe arrays at a metal interface. *Nature Materials 8*, 3 (Mar 2009), 189–193. doi: 10.1038/nmat2376.

[90] Zwerger, W. Itinerant ferromagnetism with ultracold atoms. *Science 325*, 5947 (Sep 2009), 1507. doi: 10.1126/science.1179767.

[91] Schott, S., McNellis, E. R., Nielsen, C. B., Chen, H.-Y., Watanabe, S., Tanaka, H., McCulloch, I., Takimiya, K., Sinova, J., and Sirringhaus, H. Tuning the effective spin-orbit coupling in molecular semiconductors. *Nature Communications 8*, 1 (May 2017), 15200. doi: 10.1038/ncomms15200.

[92] Kumar, A., Banerjee, K., Foster, A. S., and Liljeroth, P. Two-dimensional band structure in honeycomb metal–organic frameworks. *Nano Letters 18*, 9 (Sep 2018), 5596–5602. doi: 10.1021/acs.nanolett.8b02062.

[93] Saber, M. R., Prosvirin, A. V., Abrahams, B. F., Elliott, R. W., Robson, R., and Dunbar, K. R. Magnetic coupling between metal spins through the 7,7,8,8-tetracyanoquinodimethane (tcnq) dianion. *Chemistry – A European Journal 20*, 25 (Jun 2014), 7593–7597. doi: 10.1002/chem.201402227.

[94] Lindquist, J. M., and Hemminger, J. C. High energy resolution x-ray photoelectron spectroscopy studies of tetracyanoquinodimethane charge transfer complexes with copper, nickel, and lithium. *Chemistry of Materials 1*, 1 (Jan 1989), 72–78. doi: 10.1021/cm00001a017.

[95] Giergiel, J., Wells, S., Land, T. A., and Hemminger, J. C. Growth and chemistry of tcnq films on nickel (111). *Surface Science 255*, 1 (Sep 1991), 31–40. doi: 10.1016/0039-6028(91)90009-H.

[96] Biesinger, M. C., Payne, B. P., Lau, L. W. M., Gerson, A., and Smart, R. S. C. X-ray photoelectron spectroscopic chemical state quantification of mixed nickel metal, oxide and hydroxide systems. *Surface and Interface Analysis 41*, 4 (Apr 2009), 324–332. doi: 10.1002/sia.3026.

[97] Grosvenor, A. P., Biesinger, M. C., Smart, R. S., and McIntyre, N. S. New interpretations of xps spectra of nickel metal and oxides. *Surface Science 600*, 9 (May 2006), 1771–1779. doi: 10.1016/j.susc.2006.01.041.